

Experimental quantum computational chemistry with optimised unitary coupled cluster ansatz

Shaojun Guo,^{1,2,3,*} Jinzhao Sun,^{4,5,6,*} Haoran Qian,^{1,2,3,*} Ming Gong,^{1,2,3,*} Yukun Zhang,^{4,7} Fusheng Chen,^{1,2,3} Yangsen Ye,^{1,2,3} Yulin Wu,^{1,2,3} Sirui Cao,^{1,2,3} Kun Liu,⁴ Chen Zha,^{1,2,3} Chong Ying,^{1,2,3} Qingling Zhu,^{1,2,3} He-Liang Huang,^{1,2,3} Youwei Zhao,^{1,2,3} Shaowei Li,^{1,2,3} Shiyu Wang,^{1,2,3} Jiale Yu,^{1,2,3} Daojin Fan,^{1,2,3} Dachao Wu,^{1,2,3} Hong Su,^{1,2,3} Hui Deng,^{1,2,3} Hao Rong,^{1,2,3} Yuan Li,^{1,2,3} Kaili Zhang,^{1,2,3} Tung-Hsun Chung,^{1,2,3} Futian Liang,^{1,2,3} Jin Lin,^{1,2,3} Yu Xu,^{1,2,3} Lihua Sun,^{1,2,3} Cheng Guo,^{1,2,3} Na Li,^{1,2,3} Yong-Heng Huo,^{1,2,3} Cheng-Zhi Peng,^{1,2,3} Chao-Yang Lu,^{1,2,3} Xiao Yuan,^{4,7} Xiaobo Zhu,^{1,2,3} and Jian-Wei Pan^{1,2,3}

¹Hefei National Research Center for Physical Sciences at the Microscale and School of Physical Sciences, University of Science and Technology of China, Hefei 230026, China

²Shanghai Research Center for Quantum Science and CAS Center for Excellence in Quantum Information and Quantum Physics, University of Science and Technology of China, Shanghai 201315, China

³Hefei National Laboratory, University of Science and Technology of China, Hefei 230088, China

⁴Center on Frontiers of Computing Studies, Peking University, Beijing 100871, China

⁵QOLS, Blackett Laboratory, Imperial College London, London SW7 2AZ, United Kingdom

⁶Clarendon Laboratory, University of Oxford, Parks Road, Oxford OX1 3PU, United Kingdom

⁷School of Computer Science, Peking University, Beijing 100871, China

(Dated: June 18, 2024)

Quantum computational chemistry has emerged as an important application of quantum computing [1–7]. Hybrid quantum-classical computing methods, such as variational quantum eigensolvers (VQE) [8–10], have been designed as promising solutions to quantum chemistry problems, yet challenges due to theoretical complexity [11–14] and experimental imperfections [15] hinder progress in achieving reliable and accurate results. Experimental works for solving electronic structures are consequently still restricted to nonscalable (hardware efficient) [16, 17] or classically simulable (Hartree-Fock) ansatz [18], or limited to a few qubits with large errors [19–23]. The experimental realisation of scalable and high-precision quantum chemistry simulation remains elusive. Here, we address the critical challenges associated with solving molecular electronic structures using noisy quantum processors. Our protocol presents significant improvements in the circuit depth and running time, key metrics for chemistry simulation. Through systematic hardware enhancements and the integration of error mitigation techniques [24–28], we push forward the limit of experimental quantum computational chemistry and successfully scale up the implementation of VQE with an optimised unitary coupled-cluster ansatz to 12 qubits. We produce high-precision results of the ground-state energy for molecules with error suppression by around two orders of magnitude. We achieve chemical accuracy for H₂ at all bond distances and LiH at small bond distances in the experiment, even beyond the two recent concurrent works [29, 30]. Our work demonstrates a feasible path towards a scalable solution to electronic structure calculation, validating the key technological features and identifying future challenges for this goal.

Quantum computational chemistry, a high-potential application of quantum computing, has prompted extensive research in both theory and experiments [1–7]. Among the various approaches explored, variational quantum algorithms [8–10] emerge as a promising near-term solution with their potential for executing the task using shallow circuits. Despite the theoretical potential, due to the inherent complexity of molecular systems, quantum resources required for practical computation in terms of the gate count, measurement numbers and total running time are prohibitively large [14, 31–33]. Taking into account the noise levels (above error-correction thresholds) and limited allowed gate counts (a few hundred), achieving quantum chemistry simulation with noisy quantum processors remains elusive [12, 15]. Experiments in quantum chemistry are thus primarily restricted to proof-of-principle demonstrations with either small-scale [19–23] or limited circuit ansatz [16–18]. A notable gap exists between theoretical quantum chemistry algorithms and experimental realisations.

The pursuit of quantum computational chemistry involves addressing critical challenges related to excessive demands due to the complexity of algorithms and experimental errors. Achieving high-accuracy simulation entails the use of a more complex and expressive ansatz, which, however, introduces more errors in practice and leads to less accurate

* These authors contributed equally to this work.

results. Many existing quantum chemistry experiments are consequently restricted to either non-scalable (hardware-efficient) [16, 17] or classically simulable (Hartree-Fock) ansatz [18], which, in theory, cannot be useful for practical problems. The experimental realisation of quantum chemistry simulations is further complicated by the presence of noise [15, 34], resulting in a sense of pessimism. Even small-scale demonstrations [19–21] face significant difficulties in achieving the desired level of precision known as chemical accuracy (1.6 milli-Hartree), which is vital for reliable calculations and predictions in quantum chemistry. Significant efforts are required in protocol optimisation, hardware improvements, and effective error mitigation in order to enable scalable and high-precision experimental quantum chemistry simulation with noisy quantum processors.

In this work, we address those challenges associated with quantum chemistry simulation, and realise variational quantum eigensolver (VQE) for H_2 , LiH , and F_2 on a noisy intermediate-scale superconducting quantum processor. We consider a multi-reference initial state and develop an optimised UCC ansatz [35–37] by selecting symmetry-conserving and dominant terms. We demonstrate significant improvements in critical metrics for quantum chemistry simulation, including the circuit depth, measurement cost and total running time. On the experimental side, we developed a systematic approach aimed at optimising hardware tailored for quantum chemistry simulations. We achieved high-fidelity parallel gates leveraging the advantage of the flip-chip structure and tunable couplers, which suppress the crosstalk significantly. We introduced a calibrated implementation of basic operations in UCC-type ansatz to improve the circuit accuracy. The correlated readout error in measurements is significantly suppressed with the optimisation of readout parameters, which is verified by random state measurement. Furthermore, we designed and implemented four quantum error mitigation (QEM) protocols [24–28] to mitigate decoherence, readout, and algorithmic errors accordingly, which is crucial to obtain reliable and accurate results for chemistry applications. The efficacy of QEM in mitigating different types of errors is validated, which enables two orders of magnitude improvement of the calculation accuracy for the three molecules studied in this work. With these improvements, we can finally push forward the implementation of VQE with chemically inspired UCC ansatz and scale up the error-mitigated simulation to 12 qubits. We report that our solution allows the saturation of chemical accuracy for H_2 at all bond distances and LiH at small bond distances, with relative errors compared to initial energies less than 1.00% for all these molecules. Our work explores the potential way for scalable and reliable quantum simulation, which is a pressing and unavoidable question that arises when utilising noisy processors.

We briefly summarise the basic building blocks of our algorithm, which are outlined in Fig. 1, and refer to Supplementary Information for detailed discussions. We consider the molecular Hamiltonian under the Born-Oppenheimer approximation in second-quantisation and apply the Jordan-Wigner transformation to obtain its qubit form \hat{H} . We employ variational quantum eigensolvers to find the ground state of \hat{H} . The main idea is to prepare a parametrised quantum state $|\Psi(\boldsymbol{\theta})\rangle$ by a quantum processor and update the parameters classically. A chemically inspired choice for $|\Psi(\boldsymbol{\theta})\rangle$ is the UCC ansatz $|\Psi(\boldsymbol{\theta})\rangle = \exp(\hat{T}(\boldsymbol{\theta}) - \hat{T}^\dagger(\boldsymbol{\theta}))|\Psi_0\rangle$, which effectively considers excitations and de-excitations above a reference state $|\Psi_0\rangle$ [20–23]. Here $\hat{T}(\boldsymbol{\theta})$ is the truncated cluster operator concerning first- and second-order excitations from occupied orbitals to virtual orbitals. However, direct implementation of UCC on a quantum computer requires CNOT gates scaling as $\mathcal{O}(N(N - \eta)^2\eta^2)$ with system size N and electron number η , which goes beyond the limit of current technology.

To reduce the gate count, we design the circuit by selecting the operators from the UCC operator pool, which satisfies the symmetry constraint imposed by the selection rule [38, 39]. Moreover, since the operators in \hat{T} have different effects on the ground state [40], we select the qubit operators \hat{V} that contribute dominantly to the ground state energy decrease (see the top left column of Fig. 1 and Supplementary Section II). For instance, the total gate count is reduced by two orders of magnitude for $N = 12$. Furthermore, we compile the circuit according to the 2D topology structure of the superconducting processor to reduce the circuit depth. The gate count and circuit depth reduction strategies are scalable and essential for efficient implementations of UCC ansatz. With the ansatz state $|\Psi(\boldsymbol{\theta})\rangle$, we now aim to solve a minimisation problem, $\min_{\boldsymbol{\theta}} \langle \hat{H} \rangle_{\boldsymbol{\theta}}$, with $\langle \hat{H} \rangle_{\boldsymbol{\theta}} = \langle \Psi(\boldsymbol{\theta}) | \hat{H} | \Psi(\boldsymbol{\theta}) \rangle$. We consider a classical optimiser of stochastic gradient descent with analytical gradients obtained via a linear combination of $\langle \hat{H} \rangle_{\boldsymbol{\theta}}$ with different choices of parameters $\boldsymbol{\theta}$ [41]. Each $\langle \hat{H} \rangle_{\boldsymbol{\theta}}$ generally consists of $\mathcal{O}(N^4)$ terms, whose measurement cost could be prohibitively large in practice [32, 42]. However, as many of the observables have small coefficients and are qubit-wise compatible (hence could be measured simultaneously), more efficient measurement schemes could be exploited to alleviate the measurement cost [43, 44]. We develop an optimised overlapped grouping measurement scheme, illustrated in the top right column of Fig. 1, which reduces the required measurement count and hence the running time significantly (for instance, by two orders of magnitude for F_2 compared to importance sampling).

In order to obtain reliable experimental results, we need to optimise the quantum processor and mitigate experimental errors. In our work, various strategies are employed to improve gate operations and mitigate errors, illustrated in the bottom column of Fig. 1. We adopt dynamical decoupling [45] sequences to suppress dephasing errors for idle qubits and introduce a calibrated implementation of basic operations in UCC to improve the circuit fidelity. We further integrate error mitigation methods for the remaining measurement and gate errors. Readout error mitiga-

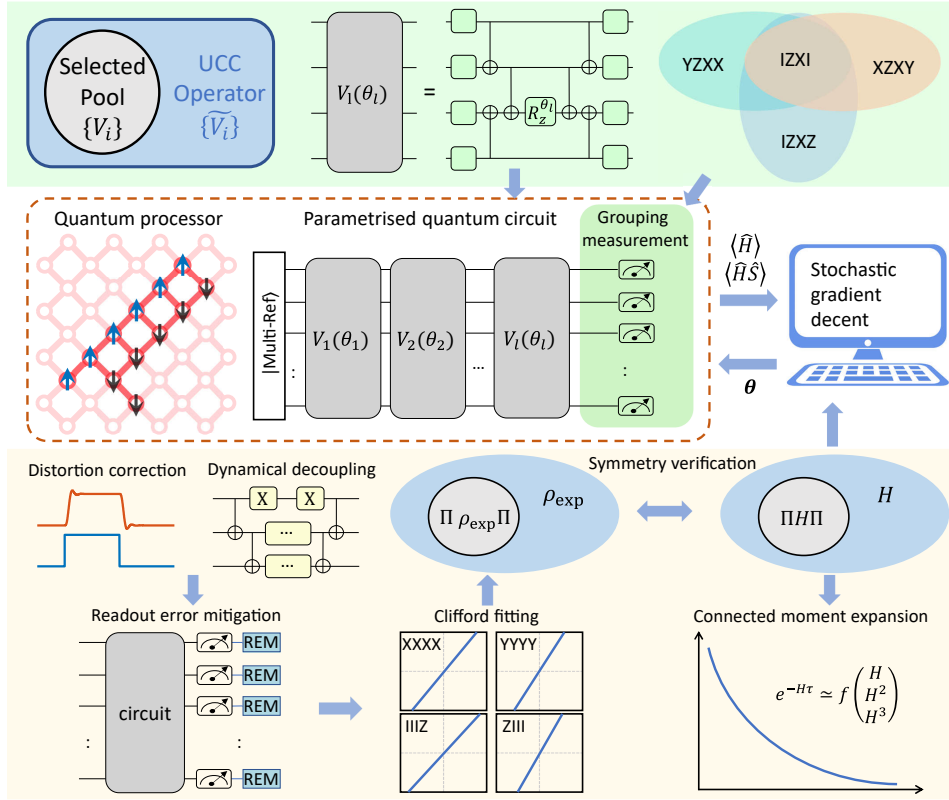


FIG. 1. **A diagrammatic scheme for the variational quantum eigensolver on a superconducting quantum processor: device, quantum circuit, measurement, and error mitigation.** Middle: The experimental circuit for 12-qubit VQE of F_2 over a 2×6 qubit grid on the “Zuchongzhi 2.0” quantum processor. Middle left: Topology of qubits on the quantum processor. The twelve selected qubits used in the experiments with the encoding of spin up and spin down are coloured. Middle right: Schematic diagram of the VQE process. Top left: Selection of the operators from the UCC operator pool that contribute dominantly to the energy decrease. Top middle: The elementary multi-qubit Pauli rotation gate in UCC, which is composed of CNOT gates, single-qubit Pauli rotation gates, and single-qubit Clifford gates. The single-qubit Pauli rotation is decomposed into a sequence of single-qubit gates R_Y - R_Z - R_Y in our experiment. Top right: An example of the overlapped grouping method for measuring observables, which exploits the qubit-wise compatibility of observables. Bottom: Hardware optimisation and error mitigation techniques integrated into the experiment. Distortion correction and dynamical decoupling are first applied to improve the fidelity of the elementary operators and suppress dephasing during idle times, respectively. Then readout error mitigation, Clifford circuit fitting, symmetry verification by parity \hat{S} , and connected moment expansion are applied sequentially to calculate the error-mitigated expectation values of observables.

tion (REM) is applied to the classical measurement outcomes to mitigate measurement errors [24]. For gate errors, we apply three types of error mitigation methods sequentially to obtain the error-mitigated expectation values of observables. Considering particle number conservation, we apply an effective symmetry verification (SV) of the particle number parity [46]; To mitigate dominant two-qubit gate errors, we apply Clifford fitting (CF) by learning the noise model from noisy and ideal Clifford circuits [25, 26]; Finally, we consider connected moment expansions (CMX), which effectively implement imaginary time evolution using Hamiltonian moments up to the third order, to correct the energy deviation due to incapable circuit ansatz and implementation errors [27, 28]. These techniques are essential for accurate experimental implementations of variational quantum algorithms.

The experiment is conducted on a 66-qubit superconducting quantum processor “Zuchongzhi 2.0” [47]. We select 12 high-quality qubits arranged in a two-dimensional array, as shown in the middle column of Fig. 1. We first optimise single-qubit gates, CZ gates and readout performance, following a series of optimisations. The readout fidelity is 96.3% on average, and the correlated readout error is verified to be negligible, characterised by random state measurements. This is achieved by optimising readout pulse and qubit frequencies, and suppressing the residual ZZ coupling (see Supplementary Information for the methods and results). The remaining uncorrelated readout errors are further alleviated by REM in our experiment. The parallel single-qubit and CZ gate fidelities are 99.90% and 99.19% on average, respectively (see Fig. 2a), characterised by cross-entropy benchmarking [48]. The high-fidelity parallel gates are achieved with the advantage of the flip-chip structure and tunable couplers, which suppresses the cross-talk error

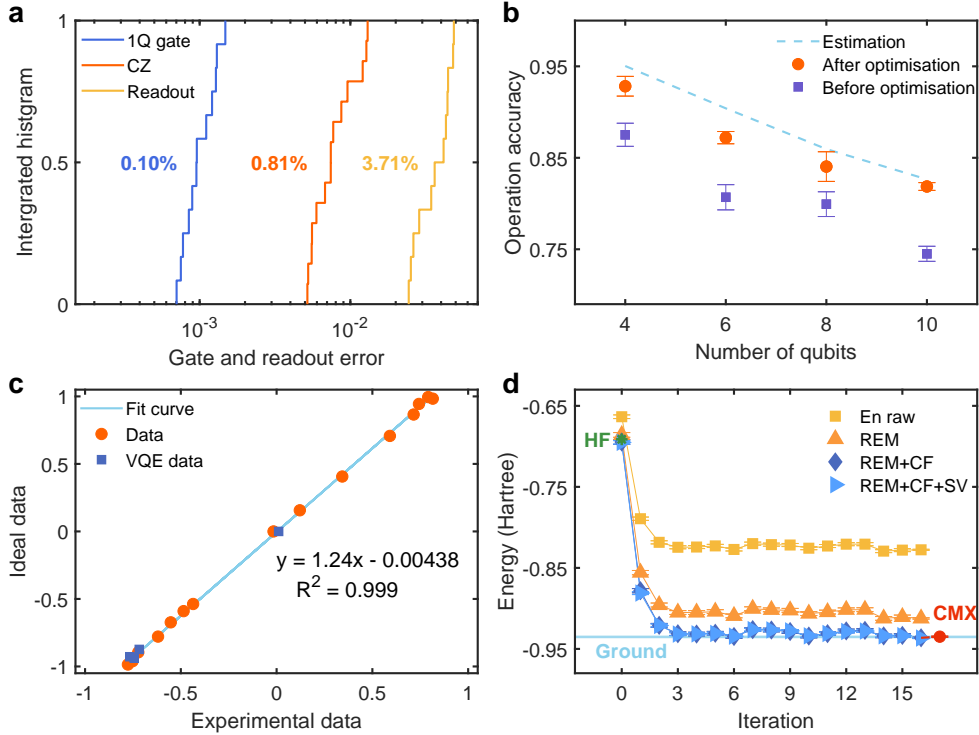


FIG. 2. **Experimental optimisation and implementation of the algorithm.** (a) Accumulated distribution of single-qubit gate (blue), CZ gate (red) and readout (yellow) errors. The number by the curve is the error on average. (b) Accuracy of multiple-qubit $\hat{V}(\theta)$ rotation gate versus the number of qubits. The operation accuracy is obtained by repeatedly executing different numbers of $\hat{V}\hat{V}^\dagger$ pairs, measuring the Z projection of all qubits, and fitting the data with an exponential function. Under the depolarising error model, the operation accuracy equals the fidelity of all quantum gates applied. The operation accuracy is closer to the direct estimation result after experimental optimisations, in which we used the $Ry(-\pi/2)$ - $Rz(\theta)$ - $Ry(\pi/2)$ gate sequence to replace the amplitude-based $Rx(\theta)$ gate and corrected the pulse distortion on relative couplers. (c) An example of Clifford fitting for H_2 with observable $XXYY$. The orange dots correspond to the ideal-noisy expectation values for Clifford-analogue circuits. The blue solid line is the linear fit of the data to learn the function, which is used to mitigate gate noise. The blue squares correspond to the ideal-noisy VQE data, which aligns well with the linear fit. (d) The optimisation procedure for H_2 with bond distance $R = 2.6$. The ground state energy with chemical accuracy (blue region) is calculated by exact diagonalisation as a benchmark. The yellow square, orange triangle, blue diamond, and grey right triangle are the energies without error mitigation, with REM, with REM + CF, and with REM + CF + SV, respectively. The red dot is the final result of the ground state energy with CMX applied.

significantly. We further optimise the elementary operations (consisting of multiple CZ gates and single-qubit gates) in the UCC circuit by correcting the Z pulse distortion on couplers and replacing the amplitude-based $Rx(\theta)$ gate. As shown in Fig. 2b, the operation accuracy notably increases after optimisation and matches the product of the fidelity of individual quantum gates, indicating its scalability for larger systems. We also highlight that the gate optimisation technique developed in this work holds potential for the preparation of multi-qubit Pauli rotation gates, which play a vital role in simulating systems with long-range interactions. All these hardware optimisations developed in our experiment are crucial for the reliable implementation of our algorithm.

To obtain high-accuracy results, we further apply three error mitigation techniques, CF, SV, and CMX, to reduce the effects of gate errors. For the observable in the Hamiltonian, we aim to obtain an error-mitigated expectation value by learning a fitting function f , which maps a noisy expectation value obtained in experiments to an error-mitigated one. To get the function f , we construct Clifford-analogue circuits of the UCC ansatz by replacing most of the non-Clifford gates with random Clifford gates. The fitting function of the new circuit instances \mathcal{S} is expected to be similar to the UCC circuit as the two-qubit gates which contribute to dominant errors are unchanged. Since Clifford circuits \mathcal{S} are classically simulable, the function f can be learned by fitting the ideal and experimental results, which are obtained by classical calculation and quantum measurements, respectively. For example, for the $XXYY$ observable in a 4-qubit H_2 -molecule case, the noisy measurement results and the ideal results have a clear linear dependence, as

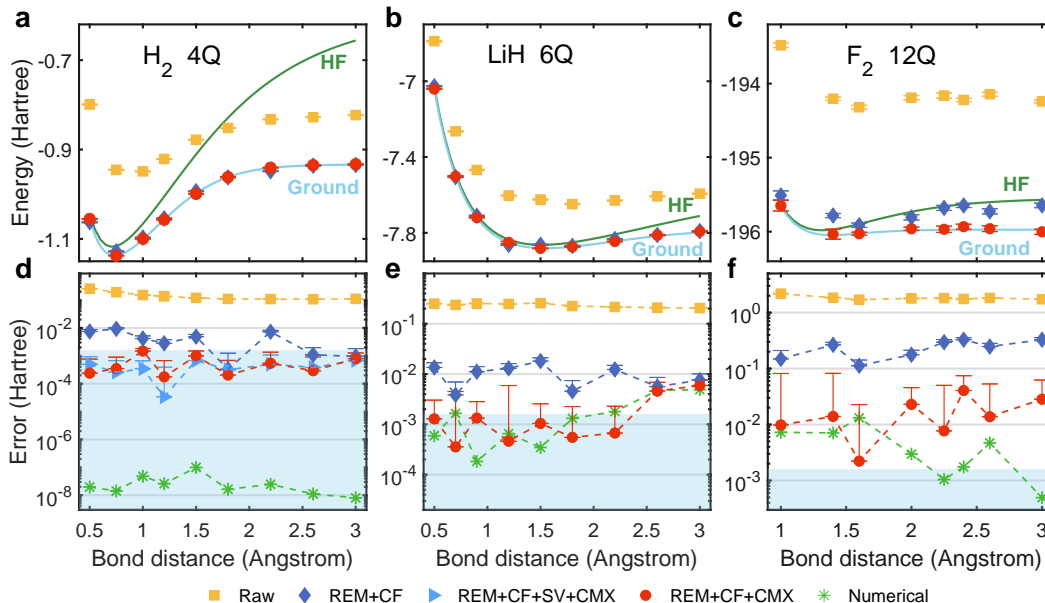


FIG. 3. **The VQE simulations for potential energy curves for different molecules.** (a-c) Potential energy curves as functions of the bond distance for H_2 (4 qubits), LiH (6 qubits) and F_2 (12 qubits) molecules with various error mitigation strategies. (d-f) Absolute errors are compared to the exact results. We compare the raw data (yellow squares) with the application of REM and CF (deep blue diamonds), SV (grey-blue triangles) and CMX (red circles). The results marked by green asterisks are energies calculated with the variational parameters searched in the experiment. The ground state energy with chemical accuracy (blue region) is calculated by exact diagonalisation as a reference.

shown in Fig. 2c. With the fitting function that is learned prior to VQE experiments, we can obtain an error-mitigated result from a given noisy measurement outcome, referred to as the CF method. During the VQE process, for each observable, we first apply REM to mitigate readout errors and then obtain an error-mitigated observable expectation value by using CF. The symmetry-verified result can be obtained by measuring additional observables $\hat{H}\hat{S}$ with the conserved symmetry \hat{S} , after which the final ground-state energy is estimated using CMX. As shown in Fig. 2d, error mitigation is critical in improving calculation accuracy. The combination of REM, CF, and SV clearly improves the energy accuracy along the optimisation iteration for the H_2 molecule. CMX further enhances the final energy within the chemical accuracy compared to the true ground state energy. The implementation and experimental comparisons of the error mitigation techniques can be found in Supplementary Section IV.

Equipped with the theoretical and experimental improvements, we now show the calculation of the potential energy curves for H_2 (4 qubits), LiH (6 qubits) and F_2 (12 qubits) molecules. The selection of active spaces and problem encoding strategies are shown in Supplementary Section II. Fig. 3 shows a significant decrease in energy errors with error mitigation (around two orders of magnitude) for all three molecules. The raw experiment results indicate that the simulation becomes less accurate with increasing system size. For instance, the raw errors for LiH and F_2 are above 0.1 Hartree and 1 Hartree, respectively. This is because VQE experiments generally entail a large number of gates and measurement shots [15, 31, 49], which results in difficulties in the demonstration of large molecular systems on current hardware. In our experiment, we improve the simulation accuracy with dedicated device optimisation and error mitigation. In particular, the average absolute energy errors for H_2 and LiH are 0.565 ± 0.542 milli-Hartree and 0.815 ± 2.526 milli-Hartree (excluding distances above 2.6 Å), respectively, which are within the chemical accuracy threshold. The energy error for LiH increases for large bond distances since UCC becomes less accurate in the dissociation regime. This has been alleviated by an optimised initial state preparation with a multi-reference state which is a superposition of the Hartree-Fock state and the dissociated state (see Supplementary Information). To validate the effectiveness of our error mitigation schemes, we compare the error-mitigated energy with the one that is computed numerically using the experimentally found parameters. The error-mitigated energies are found to be close to the numerical ones, which indicates the reliability of our scheme.

We further demonstrate the simulation for F_2 . Owing to the larger system size and deeper circuit, the energy errors for F_2 are around 10^{-2} to 10^{-1} , above the chemical accuracy threshold. The average absolute energy error for F_2 is 0.0174 ± 0.0417 Hartree. Nevertheless, if the energy is calculated using the experimentally found parameters, the energy

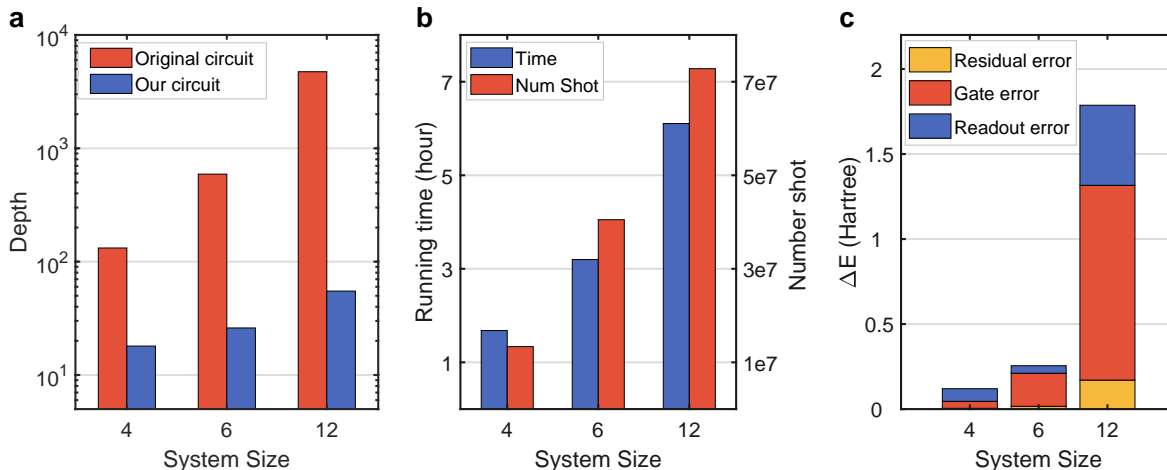


FIG. 4. **Resource estimation and error analysis with increasing system size.** (a) Circuit depth reduction. The total circuit depth is compared with the original UCCSD circuit ansatz considering single and double excitations. The total circuit depth [50] concerning both single-qubit gates and CZ gates for H_2 , LiH and F_2 are 18, 26 and 55, respectively. The number of CZ gates for H_2 , LiH and F_2 are 10, 18 and 50, respectively, and the number of single-qubit gates are 14, 19 and 63, respectively. (b) The resource estimation in terms of average running time and measurement shots of a single bond distance for the three molecules. (c) The analysis of error sources for H_2 ($R = 1.5$), LiH ($R = 1.5$) and F_2 ($R = 2.0$). Here, we denote the energy before REM, after REM, after REM and Clifford fitting, and the numerical result as E_1 , E_2 , E_3 and E_4 , respectively. The contributions from readout errors (blue), gate errors (red) and residual errors (yellow) are respectively obtained by $E_2 - E_1$, $E_3 - E_2$ and $E_4 - E_3$.

error could be consistently suppressed below 10^{-2} . The average absolute error for the numerically calculated energy is 4.81 milli-Hartree, which is 370 times smaller compared to the initial point, i.e., the experimentally measured Hartree-Fock energy. This indicates that the parameters that characterise the ground state can be found approximately, and the variational scheme is still effective, even though the error cannot be fully mitigated for deep circuits. The gate and readout fidelities need further improvements to decrease simulation error below the chemical accuracy threshold.

With the experimental results of the three molecules, we analyse the resource cost and scalability of VQE in our experiment. As shown in Fig. 4a, our circuit optimisation strategy consistently reduces the depth of UCC circuits for molecules with different system sizes. The circuit reduction strategy is efficient and crucial for extending our scheme to larger molecules. Since the VQE process essentially extracts the information from the measurement outcome, the number of measurements required is a critical concern in quantum chemistry simulation. While previous analyses of measurement resources appeared pessimistic [32, 33, 42], our optimised grouping measurement strategy significantly reduces the number of measurement bases. For instance, the number of measurements for estimating the energy of F_2 is 8.7×10^5 , with a running time of about three minutes. Comparing the three molecules in Fig. 4b, we observe that the resource cost (average running time and measurement shots) increases almost linearly in the system size. Nevertheless, we still need to be careful about device imperfections, where the primary error sources include readout and gate errors. We conduct an analysis to assess their respective contributions to the energy calculation, as shown in Fig. 4c. Our findings indicate that readout errors dominate for small molecules, while gate errors become more serious when the system size increases. Therefore, the readout and gate fidelities need to be improved systematically to achieve high accuracy for large molecules.

In this work, we demonstrate an efficient and reliable quantum chemistry solution on a noisy intermediate-scale superconducting quantum processor. We develop a systemic way to reduce quantum resources in terms of circuit depths and measurement cost, and improve our hardware in gate operations and measurement. We integrate error mitigation techniques for mitigating different types of simulation errors due to decoherence and measurement readout. With hardware optimisation tailored for chemistry simulation, we experimentally implement variational quantum eigensolvers with optimised chemically inspired ansatz and scale the simulation up to 12 qubits. Our solution enables us to achieve chemical accuracy for H_2 at all bond distances and LiH at small bond distances. We demonstrate a significant enhancement of the accuracy by around two orders of magnitude with error mitigation techniques. We examine the efficacy of error mitigation in mitigating gate and readout errors, which serves as a reference for understanding the potential benefits and limitations of error mitigation approaches, aiding in the design and optimization of future implementations.

The optimisation process in VQE imposes strict demands on the stability of quantum devices. We monitored the parameter evolution and observed its stability throughout the optimisation process over several hours, which indicates the stability of our devices as discussed in Supplementary Sections IV. While owing to non-negligible hardware errors, the current quantum processor is insufficient for larger molecules, the variational scheme is tested to be effective and reliable in our experimental implementation. Compared to the energy of the initial input state, we achieved 0.278%, 0.778%, and 1.00% relative errors for the final output states of the three molecules by applying a combination of REM, CF and CMX. We further compare the circuit error estimated using different methods to understand the effect of noise with an increasing system size. We observed that the circuit error obtained by fitting the experimental data is much lower than the error computed by multiplying the error of each individual gate, which is discussed in detail in Supplementary Section IV. Our experimental result and resource analysis indicate the potential of simulating larger molecules with improved gate and readout operations.

ACKNOWLEDGMENTS

The authors thank the USTC Center for Micro- and Nanoscale Research and Fabrication for supporting the sample fabrication. The authors also thank QuantumCTek Co., Ltd. for supporting the fabrication and maintenance of room-temperature electronics. This research was supported by the Innovation Program for Quantum Science and Technology (Grant No. 2021ZD0300200), Shanghai Municipal Science and Technology Major Project (Grant No. 2019SHZDZX01), Anhui Initiative in Quantum Information Technologies, National Natural Science Foundation of China (Grants No. 11905217, No. 11774326, No. 12175003), Natural Science Foundation of Shandong Province, China (grant number ZR202209080019), and Special funds from Jinan science and Technology Bureau and Jinan high tech Zone Management Committee. H.-L. H. acknowledges support from the Youth Talent Lifting Project (Grant No. 2020-JCJQ-QT-030), National Natural Science Foundation of China (Grants No. 11905294, 12274464), China Postdoctoral Science Foundation, and the Open Research Fund from State Key Laboratory of High Performance Computing of China (Grant No. 201901-01). J. Sun acknowledges the Samsung GRC grant for financial support. M. Gong was supported by the Youth Innovation Promotion Association of CAS (Grant No. 2022460). X.B. Zhu acknowledges support from THE XPLOER PRIZE.

AUTHOR CONTRIBUTIONS

X.Y, M.G, J.S. initiated the project. J.S. developed the theoretical aspect of the project and built up the source code for numerical simulation with input from X.Y. and Y.Z.. J.S., Y.Z, and K.L carried out the numerical simulation under the supervision of X.Y.. Y.Z. and K.L. generated the measurement bases with the algorithm developed by J.S.. S.G., H.Q., M.G., F.C. and S.C. performed the measurements. S.G., J.S., H.Q., M.G., Y.Z. analysed the experimental data. Q.Z., Y.Y., C.Y., F.C. and S.L. designed the processor. S.C., Y.L., K.Z., S.G., H.Q., T.-H.C., H.R., H.D. and Y.-H.H. fabricated the processor. M.G., S.W., C.Z., Y.Z., S.L., C.Y., J.Y., D.F., D.W. and H.S. contributed to the construction of the ultracold and low-noise measurement system. J.L., Y.X., F.L., C.G., L.S., N.L. and C.-Z.P. developed the room-temperature electronics. Experiments were performed using a quantum processor that was developed and fabricated with a large effort from the experimental team. J.S., S.G., Y.Z., X.Y. and M.G. wrote the manuscript with input from all the authors. All the authors contributed to writing up the manuscript. X.Y., X.Z., and J.-W.P. supervised the project.

Competing Interests The authors declare no competing interests.

Data and materials availability The data shown in this paper are available from the corresponding authors upon reasonable request.

Note: During the preparation of this work, we became aware of two independent works realising the unitary pair-coupled cluster double ansatz with superconducting qubits [29] and trapped ions [30], respectively, for chemical systems with the problem size at most 10 and 12 qubits. Ref. [29] showcased the efficacy of purification-based error

mitigation; however, the circuits in their experiments were produced through classical computation.

-
- [1] Alán Aspuru-Guzik, Anthony D Dutoi, Peter J Love, and Martin Head-Gordon. Simulated quantum computation of molecular energies. *Science*, 309(5741):1704–1707, 2005.
- [2] Benjamin P Lanyon, James D Whitfield, Geoff G Gillett, Michael E Goggin, Marcelo P Almeida, Ivan Kassal, Jacob D Biamonte, Masoud Mohseni, Ben J Powell, Marco Barbieri, et al. Towards quantum chemistry on a quantum computer. *Nature chemistry*, 2(2):106–111, 2010.
- [3] Javier Argüello-Luengo, Alejandro González-Tudela, Tao Shi, Peter Zoller, and J Ignacio Cirac. Analogue quantum chemistry simulation. *Nature*, 574(7777):215–218, 2019.
- [4] Markus Reiher, Nathan Wiebe, Krysta M Svore, Dave Wecker, and Matthias Troyer. Elucidating reaction mechanisms on quantum computers. *Proc. Natl. Acad. Sci. U.S.A.*, 114(29):7555–7560, 2017.
- [5] Yudong Cao, Jonathan Romero, Jonathan P. Olson, Matthias Degroote, Peter D. Johnson, Mária Kieferová, Ian D. Kivlichan, Tim Menke, Borja Peropadre, Nicolas P. D. Sawaya, Sukin Sim, Libor Veis, and Alán Aspuru-Guzik. Quantum chemistry in the age of quantum computing. *Chemical Reviews*, 119(19):10856–10915, Oct 2019.
- [6] Sam McArdle, Suguru Endo, Alán Aspuru-Guzik, Simon C. Benjamin, and Xiao Yuan. Quantum computational chemistry. *Rev. Mod. Phys.*, 92:015003, Mar 2020.
- [7] Bela Bauer, Sergey Bravyi, Mario Motta, and Garnet Kin-Lic Chan. Quantum algorithms for quantum chemistry and quantum materials science. *Chemical Reviews*, 120(22):12685–12717, 2020.
- [8] Alberto Peruzzo, Jarrod McClean, Peter Shadbolt, Man-Hong Yung, Xiao-Qi Zhou, Peter J. Love, Alán Aspuru-Guzik, and Jeremy L. O’Brien. A variational eigenvalue solver on a photonic quantum processor. *Nat. Commun.*, 5(1):4213, Jul 2014.
- [9] Marco Cerezo, Andrew Arrasmith, Ryan Babbush, Simon C Benjamin, Suguru Endo, Keisuke Fujii, Jarrod R McClean, Kosuke Mitarai, Xiao Yuan, Lukasz Cincio, et al. Variational quantum algorithms. *Nature Reviews Physics*, 3(9):625–644, 2021.
- [10] Kishor Bharti, Alba Cervera-Lierta, Thi Ha Kyaw, Tobias Haug, Sumner Alperin-Lea, Abhinav Anand, Matthias Degroote, Hermanni Heimonen, Jakob S. Kottmann, Tim Menke, Wai-Keong Mok, Sukin Sim, Leong-Chuan Kwek, and Alán Aspuru-Guzik. Noisy intermediate-scale quantum algorithms. *Rev. Mod. Phys.*, 94:015004, Feb 2022.
- [11] Seunghoon Lee, Joonho Lee, Huanchen Zhai, Yu Tong, Alexander M Dalzell, Ashutosh Kumar, Phillip Helms, Johnnie Gray, Zhi-Hao Cui, Wenyuan Liu, et al. Evaluating the evidence for exponential quantum advantage in ground-state quantum chemistry. *Nature Communications*, 14(1):1952, 2023.
- [12] Daniel Stilck França and Raul Garcia-Patron. Limitations of optimization algorithms on noisy quantum devices. *Nature Physics*, 17(11):1221–1227, 2021.
- [13] Joonho Lee, Dominic W Berry, Craig Gidney, William J Huggins, Jarrod R McClean, Nathan Wiebe, and Ryan Babbush. Even more efficient quantum computations of chemistry through tensor hypercontraction. *PRX Quantum*, 2(3):030305, 2021.
- [14] Kieran Dalton, Christopher K Long, Yordan S Yordanov, Charles G Smith, Crispin HW Barnes, Normann Mertig, and David RM Arvidsson-Shukur. Variational quantum chemistry requires gate-error probabilities below the fault-tolerance threshold. *arXiv preprint arXiv:2211.04505*, 2022.
- [15] Samson Wang, Enrico Fontana, Marco Cerezo, Kunal Sharma, Akira Sone, Lukasz Cincio, and Patrick J Coles. Noise-induced barren plateaus in variational quantum algorithms. *Nature communications*, 12(1):6961, 2021.
- [16] Abhinav Kandala, Antonio Mezzacapo, Kristan Temme, Maika Takita, Markus Brink, Jerry M Chow, and Jay M Gambetta. Hardware-efficient variational quantum eigensolver for small molecules and quantum magnets. *Nature*, 549(7671):242–246, 2017.
- [17] Abhinav Kandala, Kristan Temme, Antonio D Córcoles, Antonio Mezzacapo, Jerry M Chow, and Jay M Gambetta. Error mitigation extends the computational reach of a noisy quantum processor. *Nature*, 567(7749):491–495, 2019.
- [18] Frank Arute, Kunal Arya, Ryan Babbush, Dave Bacon, Joseph C Bardin, Rami Barends, Sergio Boixo, Michael Broughton, Bob B Buckley, David A Buell, et al. Hartree-Fock on a superconducting qubit quantum computer. *Science*, 369(6507):1084–1089, 2020.
- [19] Peter JJ O’Malley, Ryan Babbush, Ian D Kivlichan, Jonathan Romero, Jarrod R McClean, Rami Barends, Julian Kelly, Pedram Roushan, Andrew Tranter, Nan Ding, et al. Scalable quantum simulation of molecular energies. *Phys. Rev. X*, 6(3):031007, 2016.
- [20] Yangchao Shen, Xiang Zhang, Shuaining Zhang, Jing-Ning Zhang, Man-Hong Yung, and Kihwan Kim. Quantum implementation of the unitary coupled cluster for simulating molecular electronic structure. *Phys. Rev. A*, 95:020501, Feb 2017.
- [21] Cornelius Hempel, Christine Maier, Jonathan Romero, Jarrod McClean, Thomas Monz, Heng Shen, Petar Jurcevic, Ben P. Lanyon, Peter Love, Ryan Babbush, Alán Aspuru-Guzik, Rainer Blatt, and Christian F. Roos. Quantum chemistry calculations on a trapped-ion quantum simulator. *Phys. Rev. X*, 8:031022, Jul 2018.
- [22] James I Colless, Vinay V Ramasesh, Dar Dahlen, Machiel S Blok, Mollie E Kimchi-Schwartz, Jarrod R McClean, Jonathan Carter, Wibe A de Jong, and Irfan Siddiqi. Computation of molecular spectra on a quantum processor with an error-resilient algorithm. *Physical Review X*, 8(1):011021, 2018.

- [23] Yunseong Nam, Jwo-Sy Chen, Neal C Pienti, Kenneth Wright, Conor Delaney, Dmitri Maslov, Kenneth R Brown, Stewart Allen, Jason M Amini, Joel Apisdorf, et al. Ground-state energy estimation of the water molecule on a trapped-ion quantum computer. *npj Quantum Inf.*, 6(1):1–6, 2020.
- [24] Sergey Bravyi, Sarah Sheldon, Abhinav Kandala, David C. McKay, and Jay M. Gambetta. Mitigating measurement errors in multiqubit experiments. *Phys. Rev. A*, 103:042605, Apr 2021.
- [25] Piotr Czarnik, Andrew Arrasmith, Patrick J. Coles, and Lukasz Cincio. Error mitigation with clifford quantum-circuit data. *Quantum*, 5:592, nov 2021.
- [26] Angus Lowe, Max Hunter Gordon, Piotr Czarnik, Andrew Arrasmith, Patrick J Coles, and Lukasz Cincio. Unified approach to data-driven quantum error mitigation. *Physical Review Research*, 3(3):033098, 2021.
- [27] J. Cioslowski. Connected moments expansion: A new tool for quantum many-body theory. *Phys. Rev. Lett.*, 58:83–85, Jan 1987.
- [28] Daniel Claudino, Bo Peng, Nicholas P Bauman, Karol Kowalski, and Travis S Humble. Improving the accuracy and efficiency of quantum connected moments expansions. *Quantum Science and Technology*, 6(3):034012, 2021.
- [29] T. E. O’Brien, G. Anselmetti, F. Gkritis, V. E. Elfving, S. Polla, W. J. Huggins, O. Oumarou, K. Kechedzhi, D. Abanin, R. Acharya, I. Aleiner, R. Allen, T. I. Andersen, K. Anderson, M. Ansmann, F. Arute, K. Arya, A. Asfaw, J. Atalaya, J. C. Bardin, A. Bengtsson, G. Bortoli, A. Bourassa, J. Bovaird, L. Brill, M. Broughton, B. Buckley, D. A. Buell, T. Burger, B. Burkett, N. Bushnell, J. Campero, Z. Chen, B. Chiaro, D. Chik, J. Cogan, R. Collins, P. Conner, W. Courtney, A. L. Crook, B. Curtin, D. M. Debroy, S. Demura, I. Drozdov, A. Dunsworth, C. Erickson, L. Faoro, E. Farhi, R. Fatemi, V. S. Ferreira, L. Flores Burgos, E. Forati, A. G. Fowler, B. Foxen, W. Giang, C. Gidney, D. Gilboa, M. Giustina, R. Gosula, A. Grajales Dau, J. A. Gross, S. Habegger, M. C. Hamilton, M. Hansen, M. P. Harrigan, S. D. Harrington, P. Heu, M. R. Hoffmann, S. Hong, T. Huang, A. Huff, L. B. Ioffe, S. V. Isakov, J. Iveland, E. Jeffrey, Z. Jiang, C. Jones, P. Juhas, D. Kafri, T. Khattar, M. Khezri, M. Kieferová, S. Kim, P. V. Klimov, A. R. Klots, A. N. Korotkov, F. Kostritsa, J. M. Kreikebaum, D. Landhuis, P. Laptev, K.-M. Lau, L. Laws, J. Lee, K. Lee, B. J. Lester, A. T. Lill, W. Liu, W. P. Livingston, A. Locharla, F. D. Malone, S. Mandrà, O. Martin, S. Martin, J. R. McClean, T. McCourt, M. McEwen, X. Mi, A. Mieszala, K. C. Miao, M. Mohseni, S. Montazeri, A. Morvan, R. Movassagh, W. Mruczkiewicz, O. Naaman, M. Neeley, C. Neill, A. Nersisyan, M. Newman, J. H. Ng, A. Nguyen, M. Nguyen, M. Y. Niu, S. Omonije, A. Opremcak, A. Petukhov, R. Potter, L. P. Pryadko, C. Quintana, C. Rocque, P. Roushan, N. Saei, D. Sank, K. Sankaragomathi, K. J. Satzinger, H. F. Schurkus, C. Schuster, M. J. Shearn, A. Shorter, N. Shutty, V. Shvarts, J. Skrzuzny, W. C. Smith, R. D. Somma, G. Sterling, D. Strain, M. Szalay, D. Thor, A. Torres, G. Vidal, B. Villalonga, C. Vollgraf Heidweiller, T. White, B. W. K. Woo, C. Xing, Z. J. Yao, P. Yeh, J. Yoo, G. Young, A. Zalcman, Y. Zhang, N. Zhu, N. Zobrist, D. Bacon, S. Boixo, Y. Chen, J. Hilton, J. Kelly, E. Lucero, A. Megrant, H. Neven, V. Smelyanskiy, C. Gogolin, R. Babbush, and N. C. Rubin. Purification-based quantum error mitigation of pair-correlated electron simulations. *Nature Physics*, October 2023.
- [30] Luning Zhao, Joshua Goings, Kenneth Wright, Jason Nguyen, Jungsang Kim, Sonika Johri, Kyujin Shin, Woomin Kyoung, Johanna I. Fuks, June-Koo Kevin Rhee, and Young Min Rhee. Orbital-optimized pair-correlated electron simulations on trapped-ion quantum computers. *arXiv e-prints*, page arXiv:2212.02482, December 2022.
- [31] Lennart Bittel and Martin Kliesch. Training variational quantum algorithms is np-hard. *Physical review letters*, 127(12):120502, 2021.
- [32] Jérôme F. Gonthier, Maxwell D. Radin, Corneliu Buda, Eric J. Duskocil, Clena M. Abuan, and Jhonathan Romero. Measurements as a roadblock to near-term practical quantum advantage in chemistry: Resource analysis. *Phys. Rev. Res.*, 4:033154, Aug 2022.
- [33] Tzu-Ching Yen, Aadithya Ganeshram, and Artur F. Izmaylov. Deterministic improvements of quantum measurements with grouping of compatible operators, non-local transformations, and covariance estimates. *npj Quantum Information*, 9(1):14, February 2023.
- [34] Yihui Quek, Daniel Stilck França, Sumeet Khatri, Johannes Jakob Meyer, and Jens Eisert. Exponentially tighter bounds on limitations of quantum error mitigation. *arXiv preprint arXiv:2210.11505*, 2022.
- [35] Jonathan Romero, Ryan Babbush, Jarrod R McClean, Cornelius Hempel, Peter J Love, and Alán Aspuru-Guzik. Strategies for quantum computing molecular energies using the unitary coupled cluster ansatz. *Quantum Science and Technology*, 4(1):014008, 2018.
- [36] Abhinav Anand, Philipp Schleich, Sumner Alperin-Lea, Phillip WK Jensen, Sukin Sim, Manuel Díaz-Tinoco, Jakob S Kottmann, Matthias Degroote, Artur F Izmaylov, and Alán Aspuru-Guzik. A quantum computing view on unitary coupled cluster theory. *Chemical Society Reviews*, 2022.
- [37] Rodney J. Bartlett, Stanislaw A. Kucharski, and Jozef Noga. Alternative coupled-cluster ansätze II. the unitary coupled-cluster method. *Chem. Phys. Lett.*, 155(1):133–140, 1989.
- [38] John F Stanton, Jürgen Gauss, John D Watts, and Rodney J Bartlett. A direct product decomposition approach for symmetry exploitation in many-body methods. i. energy calculations. *The Journal of Chemical Physics*, 94(6):4334–4345, 1991.
- [39] Changsu Cao, Jiaqi Hu, Wengang Zhang, Xusheng Xu, Dechin Chen, Fan Yu, Jun Li, Han-Shi Hu, Dingshun Lv, and Man-Hong Yung. Progress toward larger molecular simulation on a quantum computer: Simulating a system with up to 28 qubits accelerated by point-group symmetry. *Phys. Rev. A*, 105:062452, Jun 2022.
- [40] Yi Fan, Changsu Cao, Xusheng Xu, Zhenyu Li, Dingshun Lv, and Man-Hong Yung. Circuit-depth reduction of unitary-coupled-cluster ansatz by energy sorting. *J. Phys. Chem. Lett.* 2023, 14, 43, 9596–9603, 2023.
- [41] Maria Schuld, Ville Bergholm, Christian Gogolin, Josh Izaac, and Nathan Killoran. Evaluating analytic gradients on quantum hardware. *Phys. Rev. A*, 99:032331, Mar 2019.
- [42] Dave Wecker, Matthew B. Hastings, and Matthias Troyer. Progress towards practical quantum variational algorithms.

Phys. Rev. A, 92:042303, Oct 2015.

- [43] Bujiao Wu, Jinzhao Sun, Qi Huang, and Xiao Yuan. Overlapped grouping measurement: A unified framework for measuring quantum states. *Quantum*, 7:896, 2023.
- [44] Hsin-Yuan Huang, Richard Kueng, and John Preskill. Efficient estimation of pauli observables by derandomization. *Physical review letters*, 127(3):030503, 2021.
- [45] Simon Gustavsson, Fei Yan, Jonas Bylander, Fumiki Yoshihara, Yasunobu Nakamura, Terry P. Orlando, and William D. Oliver. Dynamical decoupling and dephasing in interacting two-level systems. *Phys. Rev. Lett.*, 109:010502, Jul 2012.
- [46] X. Bonet-Monroig, R. Sagastizabal, M. Singh, and T. E. O’Brien. Low-cost error mitigation by symmetry verification. *Phys. Rev. A*, 98:062339, Dec 2018.
- [47] Yulin Wu, Wan-Su Bao, Sirui Cao, Fusheng Chen, Ming-Cheng Chen, Xiawei Chen, Tung-Hsun Chung, Hui Deng, Yajie Du, Daojin Fan, et al. Strong quantum computational advantage using a superconducting quantum processor. *Physical review letters*, 127(18):180501, 2021.
- [48] Frank Arute, Kunal Arya, Ryan Babbush, Dave Bacon, Joseph C. Bardin, Rami Barends, Rupak Biswas, Sergio Boixo, Fernando G. S. L. Brandao, David A. Buell, Brian Burkett, Yu Chen, Zijun Chen, Ben Chiaro, Roberto Collins, William Courtney, Andrew Dunsworth, Edward Farhi, Brooks Foxen, Austin Fowler, Craig Gidney, Marissa Giustina, Rob Graff, Keith Guerin, Steve Habegger, Matthew P. Harrigan, Michael J. Hartmann, Alan Ho, Markus Hoffmann, Trent Huang, Travis S. Humble, Sergei V. Isakov, Evan Jeffrey, Zhang Jiang, Dvir Kafri, Kostyantyn Kechedzhi, Julian Kelly, Paul V. Klimov, Sergey Knysh, Alexander Korotkov, Fedor Kostritsa, David Landhuis, Mike Lindmark, Erik Lucero, Dmitry Lyakh, Salvatore Mandrà, Jarrod R. McClean, Matthew McEwen, Anthony Megrant, Xiao Mi, Kristel Michielsen, Masoud Mohseni, Josh Mutus, Ofer Naaman, Matthew Neeley, Charles Neill, Murphy Yuezhen Niu, Eric Ostby, Andre Petukhov, John C. Platt, Chris Quintana, Eleanor G. Rieffel, Pedram Roushan, Nicholas C. Rubin, Daniel Sank, Kevin J. Satzinger, Vadim Smelyanskiy, Kevin J. Sung, Matthew D. Trevithick, Amit Vainsencher, Benjamin Villalonga, Theodore White, Z. Jamie Yao, Ping Yeh, Adam Zalcman, Hartmut Neven, and John M. Martinis. Quantum supremacy using a programmable superconducting processor. *Nature*, 574(7779):505–510, Oct 2019.
- [49] Jules Tilly, Hongxiang Chen, Shuxiang Cao, Dario Picozzi, Kanav Setia, Ying Li, Edward Grant, Leonard Wossnig, Ivan Rungger, George H Booth, et al. The variational quantum eigensolver: a review of methods and best practices. *Physics Reports*, 986:1–128, 2022.
- [50] The total circuit depth serves as an indicator of the system’s performance to decoherence, as in our system the time duration for single-qubit and two-qubit gates are similar.
- [51] Z. R. Lin, K. Inomata, W. D. Oliver, K. Koshino, Y. Nakamura, J. S. Tsai, and T. Yamamoto. Single-shot readout of a superconducting flux qubit with a flux-driven josephson parametric amplifier. *Applied Physics Letters*, 103(13):132602, 2013.
- [52] J. Y. Mutus, T. C. White, R. Barends, Yu Chen, Z. Chen, B. Chiaro, A. Dunsworth, E. Jeffrey, J. Kelly, A. Megrant, C. Neill, P. J. J. O’Malley, P. Roushan, D. Sank, A. Vainsencher, J. Wenner, K. M. Sundqvist, A. N. Cleland, and John M. Martinis. Strong environmental coupling in a josephson parametric amplifier. *Applied Physics Letters*, 104(26):263513, 2014.
- [53] Zhiguang Yan, Yu-Ran Zhang, Ming Gong, Yulin Wu, Yarui Zheng, Shaowei Li, Can Wang, Futian Liang, Jin Lin, Yu Xu, Cheng Guo, Lihua Sun, Cheng-Zhi Peng, Keyu Xia, Hui Deng, Hao Rong, J. Q. You, Franco Nori, Heng Fan, Xiaobo Zhu, and Jian-Wei Pan. Strongly correlated quantum walks with a 12-qubit superconducting processor. *Science*, 364(6442):753–756, 2019.
- [54] Yangsen Ye, Sirui Cao, Yulin Wu, Xiawei Chen, Qingling Zhu, Shaowei Li, Fusheng Chen, Ming Gong, Chen Zha, He-Liang Huang, Youwei Zhao, Shiyu Wang, Shaojun Guo, Haoran Qian, Futian Liang, Jin Lin, Yu Xu, Cheng Guo, Lihua Sun, Na Li, Hui Deng, Xiaobo Zhu, and Jian-Wei Pan. Realization of high-fidelity controlled-phase gates in extensible superconducting qubits design with a tunable coupler. *Chinese Physics Letters*, 38(10):100301, nov 2021.
- [55] Youngkyu Sung, Leon Ding, Jochen Braumüller, Antti Vepsäläinen, Bharath Kannan, Morten Kjaergaard, Ami Greene, Gabriel O. Samach, Chris McNally, David Kim, Alexander Melville, Bethany M. Niedzielski, Mollie E. Schwartz, Jonilyn L. Yoder, Terry P. Orlando, Simon Gustavsson, and William D. Oliver. Realization of high-fidelity cz and zz-free iswap gates with a tunable coupler. *Phys. Rev. X*, 11:021058, Jun 2021.
- [56] Julian Kelly, Peter O’Malley, Matthew Neeley, Hartmut Neven, and John M Martinis. Physical qubit calibration on a directed acyclic graph. *arXiv preprint arXiv:1803.03226*, 2018.
- [57] Qiming Sun, Timothy C Berkelbach, Nick S Blunt, George H Booth, Sheng Guo, Zhendong Li, Junzi Liu, James D McClain, Elvira R Sayfutyarova, Sandeep Sharma, et al. Pyscf: the python-based simulations of chemistry framework. *Wiley Interdisciplinary Reviews: Computational Molecular Science*, 8(1):e1340, 2018.
- [58] Dave Wecker, Matthew B. Hastings, and Matthias Troyer. Progress towards practical quantum variational algorithms. *Phys. Rev. A*, 92:042303, Oct 2015.
- [59] Joonho Lee, William J Huggins, Martin Head-Gordon, and K Birgitta Whaley. Generalized unitary coupled cluster wave functions for quantum computation. *Journal of chemical theory and computation*, 15(1):311–324, 2018.
- [60] Nicholas C. Rubin, Klaas Gunst, Alec White, Leon Freitag, Kyle Throssell, Garnet Kin-Lic Chan, Ryan Babbush, and Toru Shiozaki. The fermionic quantum emulator. *Quantum*, 5:568, Oct 2021.
- [61] Kosuke Mitarai, Makoto Negoro, Masahiro Kitagawa, and Keisuke Fujii. Quantum circuit learning. *Physical Review A*, 98(3):032309, 2018.
- [62] Andrea Mari, Thomas R Bromley, and Nathan Killoran. Estimating the gradient and higher-order derivatives on quantum hardware. *Physical Review A*, 103(1):012405, 2021.
- [63] Charles Hadfield, Sergey Bravyi, Rudy Raymond, and Antonio Mezzacapo. Measurements of quantum hamiltonians with

- locally-biased classical shadows. Communications in Mathematical Physics, 391(3):951–967, 2022.
- [64] Sergey Bravyi, Sarah Sheldon, Abhinav Kandala, David C McKay, and Jay M Gambetta. Mitigating measurement errors in multiqubit experiments. Phys. Rev. A, 103(4):042605, 2021.
- [65] Piotr Czarnik, Andrew Arrasmith, Patrick J Coles, and Lukasz Cincio. Error mitigation with clifford quantum-circuit data. Quantum, 5:592, 2021.
- [66] Sergey Bravyi, Dan Browne, Padraic Calpin, Earl Campbell, David Gosset, and Mark Howard. Simulation of quantum circuits by low-rank stabilizer decompositions. Quantum, 3:181, 2019.
- [67] Karol Kowalski and Bo Peng. Quantum simulations employing connected moments expansions. The Journal of Chemical Physics, 153(20):201102, 2020.

SUPPLEMENTARY INFORMATION

CONTENTS

Acknowledgments	7
Author contributions	7
References	8
Supplementary Information	12
I. Device and calibration	12
A. Device	12
B. System calibration	13
C. Multi-qubit Pauli rotation gate calibration and optimisation	14
D. Correlated readout error and random state measurements	17
II. Variational quantum state preparation and measurement	18
A. Problem encoding and qubit reduction	18
B. Initial state preparation	18
C. Quantum circuit ansatz design and compilation	20
1. Unitary coupled cluster circuit ansatz	20
2. Point group symmetry constraint	21
3. Selection of excitation operators	22
4. Quantum circuit compilation	23
D. Optimisation by analytic stochastic gradient descent	24
E. Quantum state measurement and classical post-processing	26
1. Overlapped grouping measurement	26
2. Optimisation process	27
III. Error-mitigated observable estimation	28
A. Readout error mitigation	28
B. Gate error learning by Clifford fitting	30
1. Methods	30
2. Experimental procedure	30
C. Symmetry verification	31
D. Connected moments expansion	32
E. Experimental procedure for observable estimation	33
IV. Experimental implementation and results	33
A. Experimental procedure	33
B. Results	36
C. Parameters iteration	38
D. Noise analysis	39
E. Challenges	39

I. DEVICE AND CALIBRATION

A. Device

The “Zuchongzhi 2.0” quantum processor contains 66 qubits and 110 couplers. In order to control and wire such a large-scale quantum processor, the qubit layer and wiring layer are prepared on separate chips, which are then combined using the flip-chip packaging process. High-purity aluminium thin films are grown on a sapphire substrate by molecular beam epitaxy (MBE) for both chips, which can reduce material loss and improve qubit decoherence performance. The wiring layer employs photolithography and etching processes to fabricate readout circuits and control circuits and utilizes a lift-off process for creating airbridges. These airbridges effectively establish grounding

connections, which prevent slot line modes, and simultaneously reduce crosstalk between control circuits. This results in superior qubit isolation and enables high-precision gate operations. The qubits and couplers are fabricated on the qubit layer. In this process, the capacitive elements of the qubits and couplers are defined using photolithography and etching. The Josephson junction is created by defining the junction area using electron beam equipment and then prepared using a dual-angle evaporation process followed by a lift-off process. During the fabrication process, we fine-tuned the junction’s critical current by adjusting the oxidation conditions and the size of the junction region. This allowed us to achieve the optimal frequency adjustment range for both qubits and couplers. Furthermore, a considerable number of indium bumps as superconducting interconnects are employed to establish a solid ground connection between the qubit layer and the wiring layer, effectively reducing parasitic modes.

Following the chip fabrication process, the processor is wire-bonded to a printed circuit board located within a sample box. This sample box is equipped with gold-plated shielding inside and μ -metal shielding outside. Finally, the packaged processor is mounted to the plate of a dilution refrigerator and connected to room-temperature electronics via a series of attenuators, filters, and amplifiers.

B. System calibration

Our experiment is carried out on the “Zuchongzhi 2.0” quantum processor. We selected up to 12 qubits to run the quantum circuits. We turned off the coupling between used and unused qubits. Then, we optimised and calibrated the performance of the selected qubits, especially the quantum gates and readout performance.

The optimisation procedure of our quantum processor can be summarised into the following steps:

1. **Select idle frequencies.** Idle frequencies refer to the qubit operating frequencies when the qubits are in idle operations or single-qubit gates. As the qubit performance varies strongly with the frequency, setting the qubits in good idle frequencies is necessary to achieve high-fidelity gates. To arrange the idle frequencies, we need to consider a combination of factors, including coherence time, residual coupling between qubits, the distance between idle frequencies and CZ interaction frequencies (related to z distortions), two-level systems (TLSs), and XY-crosstalk. XY-crosstalk comes from the interaction between control lines and the distance of the driven frequencies.
2. **Turn off the coupling between qubits.** In the setting of idle frequencies, the frequency distance between nearest-neighbour qubits is about 100MHz. Turning off the coupling to suppress the interaction between qubits is necessary to decrease parallel-gate errors. After setting qubit idle frequencies, we determine the coupler zero-coupling point by measuring the relative two-qubit conditional phase when varying the flux of the coupler. Then, we turn off the qubit-qubit coupling by adjusting the coupler flux bias to the selected zero-coupling point.
3. **Optimise single-qubit gates.** We fine-tune the XY drive pulse amplitudes and apply Derivative Reduction by Adiabatic Gate (DRAG) correction to the pulse envelope with a length of 25 ns.
4. **Optimise the Josephson Parametric Amplifiers (JPAs).** The JPA can significantly improve the readout signal-to-noise ratio (SNR) and fidelity [51, 52]. First, we coarsely tune the JPA direct current (DC) bias, pump signal power and frequency according to our design. Then, these parameters are optimised by the Nelder–Mead algorithm, and the target function is the average SNRs of the qubit readout signals.
5. **Optimise the pulse distortion of each qubit.** Distortion or reflection occurs when the pulse is transmitted from a waveform generator to qubits, and it will cause a shift in the qubit frequency which increases the gate error in the quantum circuit. In our experiment, we first measure the effect of pulse distortion on qubit phase accumulation over a fixed time of 400 ns. Then we calculate the waveform after distortion based on the result of phase accumulation and apply a reverse one to compensate for the pulse. The full protocol is detailed in Ref [53]
6. **Optimise the readout crosstalk.** Readout crosstalk may be generated by factors such as the influence of neighbouring qubits on readout ones, coupling between readout resonators, frequency collision (caused by the overlap of demodulation frequencies, intermodulation of parametric amplifiers, etc.). It can reduce the readout fidelity and make REM unreliable. The readout crosstalk can be well suppressed by optimising the readout parameters, including frequencies and lengths of readout signal and qubits’ frequencies for readout.
7. **Calibrate the readout performance.** After optimising the readout crosstalk, we need to confirm whether residual crosstalk is negligible. Here, we first calibrate the standard readout fidelity with qubits preparing in $|0\rangle^{\otimes n}$ and $|1\rangle^{\otimes n}$. Then, we prepare the qubits in a random state set and calibrate the readout fidelity again. If the fidelities are close in both cases, the residual crosstalk is negligible.

8. **Optimise CZ gates.** In the UCC ansatz, the multi-qubit Pauli rotation gate $\hat{V}(\boldsymbol{\theta})$ is an elementary operator, which is compiled with single-qubit gates and CZ gates. The CZ gate with tunable-coupler structure has been investigated and realised with high fidelity [54, 55]. In our experiment, CZ gates are realised by utilising the resonance coupling between $|11\rangle$ and $|02\rangle$ states and optimised by the following steps:

- (a) According to the pattern in circuits, The CZ gates and single-qubit gates are divided into different groups. The next steps will be performed individually in these groups.
- (b) We collect coherence information (T1 and T2) for a large frequency range ($\sim 100\text{MHz}$) of qubits and determine the frequency region that is suitable for CZ interaction accordingly.
- (c) We first prepare the qubits in $|11\rangle$ states. Then, we measure the conditional phase with varying coupling strength (tuning by coupler) for a fixed 50 ns gate time. Next, we measure the leakage of qubit states to $|02\rangle$ or $|20\rangle$ as qubit interaction frequencies vary. Finally, we coarsely determine the interaction frequencies and coupling strengths by minimising the cost function of conditional phase error and leakage error.
- (d) Select a CZ gate in the group and finely adjust its parameters by optimising the XEB (cross-entropy benchmarking) fidelity with a fixed cycle of 20 and fixed random circuits of 60 while keeping other parameters of the CZ gate unchanged.
- (e) We repeat step (d) for the CZ gate with the lowest fidelity in the group until the average fidelity no longer improves.

9. **Calibrate single-qubit gates and CZ gates.** We utilise the SPB and XEB measurements to calibrate single-qubit and CZ gates. For CZ gates, the dynamical phases on both qubits are also determined in the XEB experiment.

All steps can be realised automatically as a directed graph [56], except for step 6, which needs to be checked manually. We refer to Ref. [47] for more details about the performance calibration of quantum devices.

After all the calibrations and optimisations, we summarised the qubit parameters in Fig. 5, and the errors for single-qubit gates, two-qubit gates and readout in Fig. 2a in the main text and Fig. 6. Fig. 2a in the main text shows the accumulated distribution of single-qubit gate, CZ gate and readout errors. Fig. 6 shows the spatial distribution of those gate errors for selected qubits on the ‘‘Zuchongzhi 2.0’’ quantum processor. There is no strong spatial error distribution in our qubit set. We run the automatic calibration steps 3, 7, 8, and 9 every three hours to maintain the system’s performance.

C. Multi-qubit Pauli rotation gate calibration and optimisation

The multi-qubit Pauli rotation gate $\hat{V}(\boldsymbol{\theta})$ is an elementary operator in the UCC ansatz. Consequently, the quality of $\hat{V}(\boldsymbol{\theta})$ directly determines the accuracy of our VQE experiment. In addition to high-fidelity single-qubit and CZ gates, two more experimental improvements are made to increase the quality of $\hat{V}(\boldsymbol{\theta})$.

The Z-pulse distortion on the couplers could lead to a non-ideal coupling strength during the CZ gate and cause a residual wave trailing after the gate. Since $\hat{V}(\boldsymbol{\theta})$ is mainly composed of CZ gates, a non-ideal transmission characteristic will generate unwanted pulse distortion, thus increasing the error of the following gates. The residual effect is difficult to observe in the two-qubit XEB experiment. However, the trailing signal on the coupler will shift the qubit frequencies and reduce the fidelity of the gates in multi-qubit Pauli rotation. We first correct the Z-pulse distortion on the coupler to address this problem. We apply the Z waveform to the couplers and measure the phase accumulation of the adjacent coupled qubit. With the relation between coupler Z bias amplitude and qubit frequency, we could calculate the response function of the coupler control line, thereby achieving the correction through reverse waveform compensation.

Secondly, $R_x(\boldsymbol{\theta})$ in $\hat{V}(\boldsymbol{\theta})$ is a non-Clifford gate, with different rotating angles originally realised with different pulse amplitude by linear adjustment. The error of $R_x(\boldsymbol{\theta})$ is significantly larger than a standard single-qubit gate due to a non-linear response nonlinear response in the signal generation and transformation. On the other hand, the DRAG parameters are calibrated using $\pi/2$ gate, a fixed DRAG parameter for an arbitrary rotation gate $R_x(\boldsymbol{\theta})$ would lead to additional control error and state leakage. Therefore, we replace the $R_x(\boldsymbol{\theta})$ with $R_y(-\pi/2)R_z(\boldsymbol{\theta})R_y(\pi/2)$. In our experiment, $R_z(\boldsymbol{\theta})$ is a virtual gate. This replacement reduces the error of $R_x(\boldsymbol{\theta})$ and guarantees the performance of Clifford fitting, which highly relies on the control accuracy in $R_x(\boldsymbol{\theta})$, as introduced in Sec. III B.

We benchmark the operation quality with and without the above two improvements by the following protocol:

1. Initialise all qubits in the state $|0\rangle^{\otimes n}$.

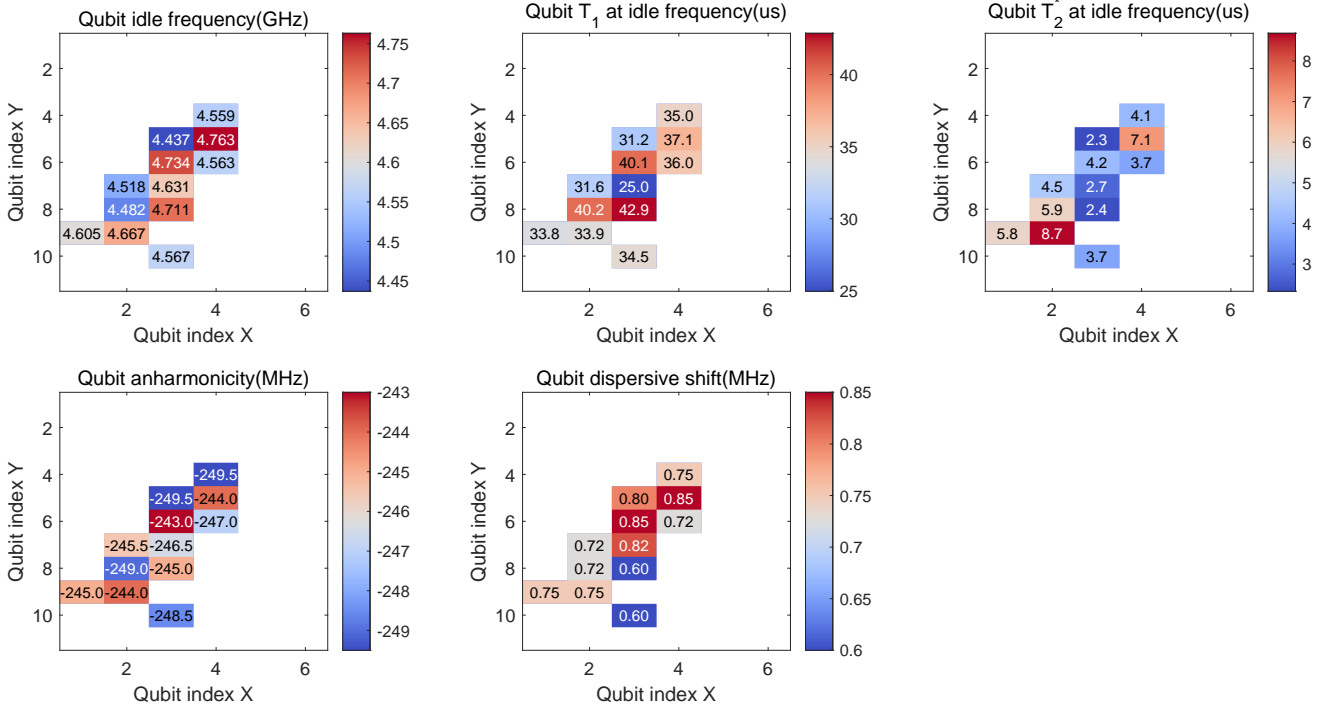


FIG. 5. **The typical distribution of the qubit parameters.** Idle frequency, T_1 , T_2^* , anharmonicity and dispersive shift for the selected 12 qubits.

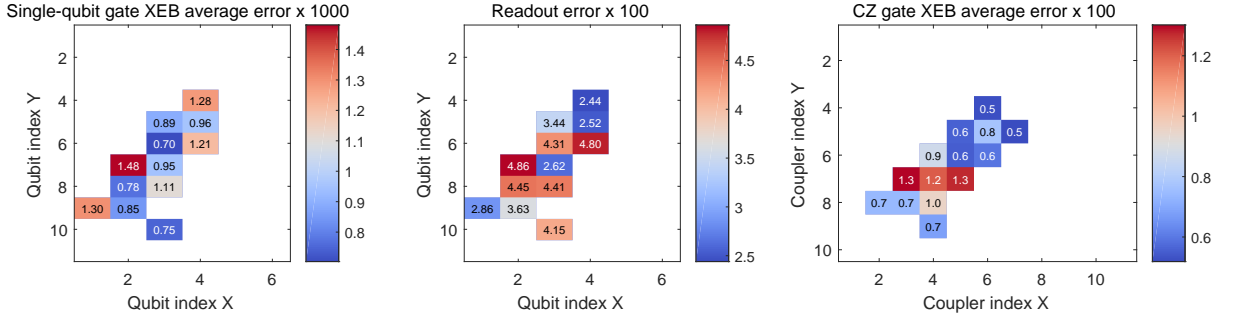


FIG. 6. **The performance of the quantum processor after calibration.** Error for readout, single-qubit, and CZ gates for the selected 12 qubits.

2. Apply a sequence consisting of m sets of $\hat{V}\hat{V}^\dagger$ pairs with different random-selected rotating angle θ .
3. Perform projection measurements along the Z direction to obtain the projection probability to $|0\rangle^{\otimes n}$.
4. Repeat steps 2 and 3 for k times to obtain a stable average probability.
5. Change the length m and repeat steps 2, 3 and 4.

Note that when the noise is sufficiently small, $\hat{V}\hat{V}^\dagger$ should be close to identity, and hence the projection probability should be close to 1. Therefore, the projection probability value reflects the implemented gate's quality. Let us denote the implemented noisy gates as \tilde{V} and \tilde{V}^\dagger . Here, in order to see a more explicit relation, we make the following assumptions:

1. The implemented noisy gates \tilde{V} and \tilde{V}^\dagger are the corresponding noiseless gates V and V^\dagger concatenated by an error process $\mathcal{E}(\rho)$.

2. The error process \mathcal{E} of the implemented noisy \tilde{V} is gate-independent, time-independent, and parameter-independent, and can be described by a depolarising channel $\mathcal{E}(\rho) = p\rho + (1-p)I/2^n$ with the identity operation I and the error rate $1-p$.

Under the above assumptions, the averaged gate fidelity of the noisy \tilde{V} is

$$F_{\text{avg}} = \int d\psi \text{Tr}[\mathcal{V}(\psi)\tilde{\mathcal{V}}(\psi)] \approx p \quad (1)$$

Here $\mathcal{V}(\cdot) = \hat{V}(\cdot)\hat{V}^\dagger$, $\tilde{\mathcal{V}}(\cdot) = \tilde{V}(\cdot)\tilde{V}^\dagger$, and we have neglected exponential dependence of $\mathcal{O}(1/2^n)$.

Now, consider m sets of noisy $\tilde{V}\tilde{V}^\dagger$ on $\rho_0 = |\bar{0}\rangle\langle\bar{0}|$, we have

$$\rho = \prod_{i=1}^m \mathcal{E}\mathcal{V}^\dagger\mathcal{E}\mathcal{V}(\rho_0) = p^{2m}\rho_0 + (1-p^{2m})I/2^n. \quad (2)$$

The probability to obtain $|\bar{0}\rangle\langle\bar{0}|$ is given by $\text{Tr}(|\bar{0}\rangle\langle\bar{0}|\rho) \approx p^{2m}$, where we again neglect exponential small dependence of $\mathcal{O}(1/2^n)$. Considering state preparation and measurement errors (assuming the stochastic noise model), we can show that the expectation value of Z takes the form of $Ap^{2m} + B$. Therefore, the error rate p can be obtained by fitting the measurement outcomes with different choices of m .

In the experiment, we use the fitting curve as a benchmark of the noisy $\tilde{V}(\theta)$, as shown in Fig. 7. This figure clearly shows the difference in the quality before and after optimisation for the number of qubits as 4, 6, 8 and 10. After optimisation, there is an average 6% improvement for the $\tilde{V}(\theta)$ gate. This experiment demonstrates a fast, scalable, and efficient protocol to benchmark a multi-qubit quantum computational chemistry operation.

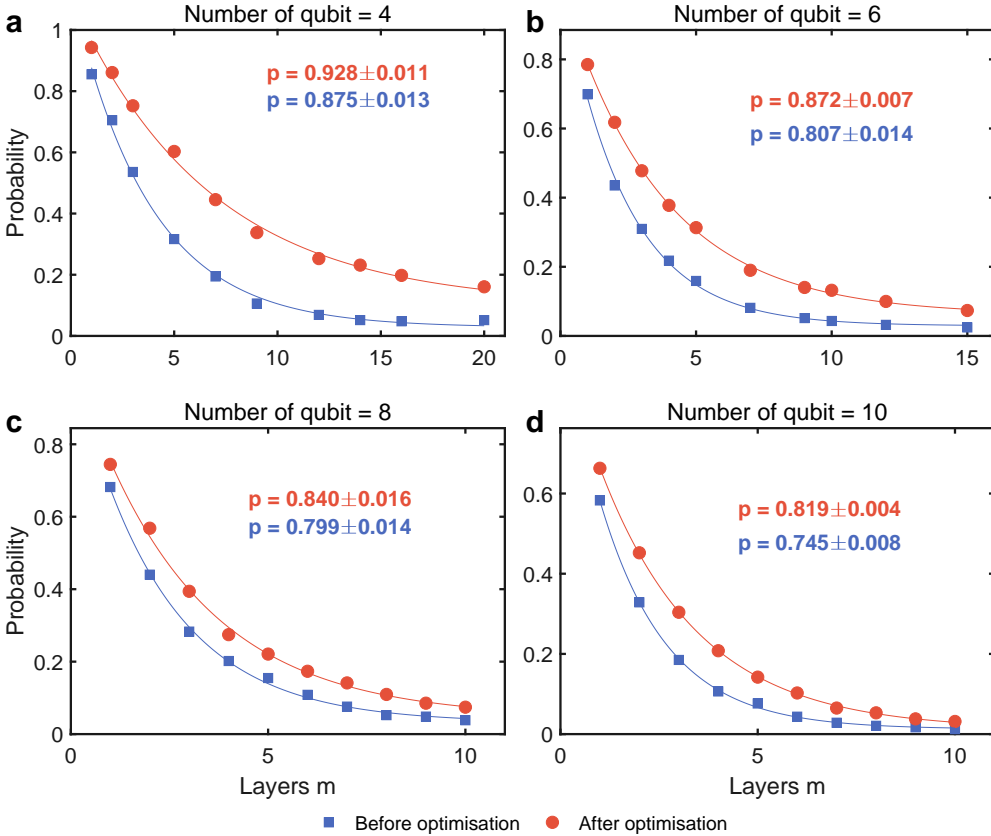


FIG. 7. **Benchmark of multi-qubit Pauli rotation gate.** The error rate of each sequence, as a characteristic of the averaged fidelity, can be obtained by measuring the probability of $|0\rangle^{\otimes n}$. The data points are the average values at each sequence length.

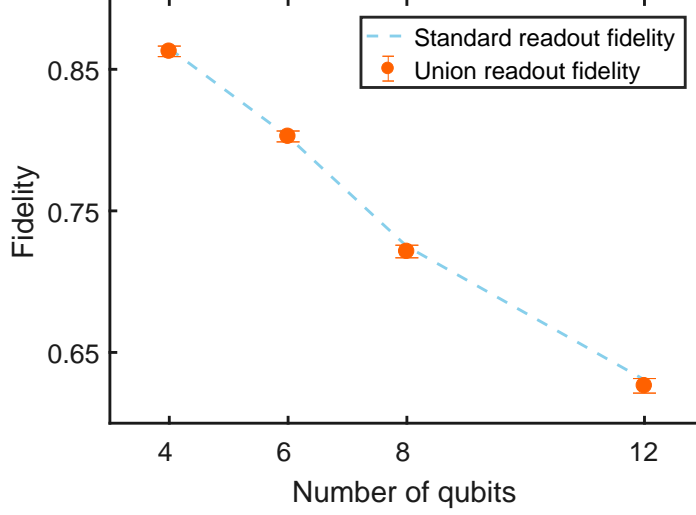


FIG. 8. **Union readout fidelity.** Comparison of average union readout fidelity (orange dots) and standard readout fidelity (blue dashed line) for four qubits, six qubits, eight qubits and twelve qubits.

D. Correlated readout error and random state measurements

Quantum state measurements determine the information that we can extract from quantum experiments. Measurement errors can significantly impact simulation accuracy since they introduce a bias in the expectation value. Therefore, it is essential to mitigate measurement errors to ensure reliable results.

To mitigate measurement errors, the first step is to learn the measurement noise matrix Λ from readout calibration measurements. Provided an invertible measurement noise matrix Λ , we can mitigate measurement readout errors by applying an inverse matrix Λ^{-1} to the noisy measurement outcomes.

There are two types of measurement calibration matrices, one takes a tensor product form, a tensor product of local single-qubit calibration matrices, while the other one characterises correlated noise. The latter requires more experimental resources, which is not desirable in experiments. When the correlated readout error is negligible, noise can be well described by a measurement noise matrix with a tensor product form.

In general, correlated readout error arises from the residual coupling and the spectral overlap of readout resonators. We make two improvements to ensure that the correlations of measurement errors are weak enough to be neglected.

Firstly, we suppressed the residual coupling by adjusting the working point of the coupler delicately. Secondly, we optimised readout parameters simultaneously, including readout pulse frequencies, readout pulse amplitudes, readout pulse length and qubit readout frequencies.

After these improvements, we verified the correlated readout error was suppressed by comparing the results of standard measurement and random state measurement. The verification by in the following steps:

1. Prepare all qubits in $|0\rangle^{\otimes n}$ and $|1\rangle^{\otimes n}$ to acquire F_{00} and F_{11} . Here, F_{00} (F_{11}) means the probability to get a measure result of $|0\rangle$ ($|1\rangle$) when the qubit was prepared in $|0\rangle$ ($|1\rangle$).
2. Random state measurements. Randomly prepare the qubit state and use the same discrimination line of the readout signal demodulated IQ clouds to calculate fidelity. Multiply the fidelities for all qubits, and we refer to the multiplication as the union readout fidelity.
3. With hundreds of repeated experiments, averaged union readout fidelity is computed.

Fig. 8 compares the average standard and union readout fidelity. These two types of readout fidelity show a good agreement, and the correlated readout error is negligible, which ensures the tensor product form is applicable in this experiment.

II. VARIATIONAL QUANTUM STATE PREPARATION AND MEASUREMENT

This section discusses quantum algorithms for quantum chemistry problems, including variational state preparation, optimisation, and quantum state measurement. This section is organised as follows. In [Sec. II B](#), we first demonstrate multi-reference state preparation on a quantum processor and illustrate the corresponding circuit. In [Sec. II C](#), we introduce quantum circuit design strategies based on unitary coupled cluster ansatz, and propose a circuit reduction strategy to enable the simulation on current hardware. Quantum circuits for the three molecules are shown in [Sec. II C 4](#). In [Sec. II D](#), we introduce an optimisation scheme by analytic stochastic gradient descent and present the analytical form of the gradient estimation. In [Sec. II E](#), we introduce an efficient quantum state measurement strategy for measuring multiple observables.

A. Problem encoding and qubit reduction

This work considers second-quantised molecular Hamiltonians represented in a discrete basis set in the active space. We implement qubit reduction by separating the full space of molecular orbitals into three parts: the core, active, and virtual space. We select the core orbitals as those that stay chemically inert. That is, their occupation numbers are sufficiently close to two when expanding the ground state of the Hamiltonian as a linear combination of Slater determinants, and virtual orbitals as those whose occupation numbers are close to zero. By classifying molecular orbitals into these three categories, we only need to compute the ground state in the selected active space, and thus the number of qubits required is reduced. As discussed in Ref. [6], a generic way to determine the classification of molecular orbitals is by computing the one-particle reduced density matrix (1-RDM) using an approximation of the ground state generated by a classical tractable method, such as the coupled cluster method. The 1-RDM is defined as ${}^1D_j^i = \langle \hat{a}_i^\dagger \hat{a}_j \rangle$. By diagonalising the 1-RDM by a basis rotation operation, we obtain the natural orbital occupied numbers (NOONs) for every molecular orbital. NOON indicates the expected occupation number for the corresponding orbital, based on which we can determine the core, active and virtual spaces by the pre-determined thresholds.

We show the irreducible representations (irreps) of orbitals in the selected active space for the molecules that are considered in this work. The Hamiltonians for various molecules are generated in the minimal basis set, known as the STO-3G basis, using the PySCF package [57]. For the H_2 molecule, we do not implement qubit reduction. The irreps of Hartree Fock orbitals of the LiH and F_2 molecules at different bond distances are plotted in [Fig. 9](#). The point group of the LiH molecule is $C_{\infty v}$. Four Hartree Fock orbitals of LiH are of irreps a_1 and the other two are of e_1 . We freeze the lowest orbitals with $1a_1$ and $2a_1$ irreps, and remove the orbitals with $1e_1$ and $2e_1$ irreps. The point group of F_2 is $D_{\infty h}$. We freeze the four lowest core orbitals with irreps $1a_1$, $2a_1$, $3a_1$ and $4a_1$. The other orbitals of $1e_1$, $2e_1$, $3e_1$, $4e_1$, $5a_1$ and $6a_1$ irreps are selected in the active space.

With the selected orbitals in the active space, these molecular Hamiltonian can be expressed in the second quantisation as

$$\hat{H} = \sum_{i,j} h_{ij} \hat{a}_i^\dagger \hat{a}_j + \frac{1}{2} \sum_{i,j,k,l} g_{ijkl} \hat{a}_i^\dagger \hat{a}_j^\dagger \hat{a}_k \hat{a}_l, \quad (3)$$

where \hat{a}_i^\dagger and \hat{a}_i denote the fermionic creation and annihilation operators associated with i th molecular orbitals in the active space, respectively. The coefficients h_{ij} and g_{ijkl} are the one- and two-electron integrals that can be evaluated classically provided the spin-orbital basis function.

Under the Jordan-Wigner transformation, the fermionic Hamiltonian can be mapped to a qubit form which is suitable for evaluation on a quantum processor. The Jordan-Wigner transformation maps the fermionic operators \hat{a}_j and \hat{a}_j^\dagger on each fermionic mode to the qubit Pauli operators as

$$\hat{a}_j \mapsto \frac{1}{2} (X_j + iY_j) \bigotimes_{i=1}^{j-1} Z_i, \quad \hat{a}_j^\dagger \mapsto \frac{1}{2} (X_j - iY_j) \bigotimes_{i=1}^{j-1} Z_i \quad (4)$$

with Pauli operators X , Y , Z acting on the j th qubit.

B. Initial state preparation

As the spin Hamiltonian is constructed according to the $SU(2)$ symmetry, we consider the initial state or the reference state obeying this symmetry by assigning an equal number of electrons to the spin α and β sectors. Also,

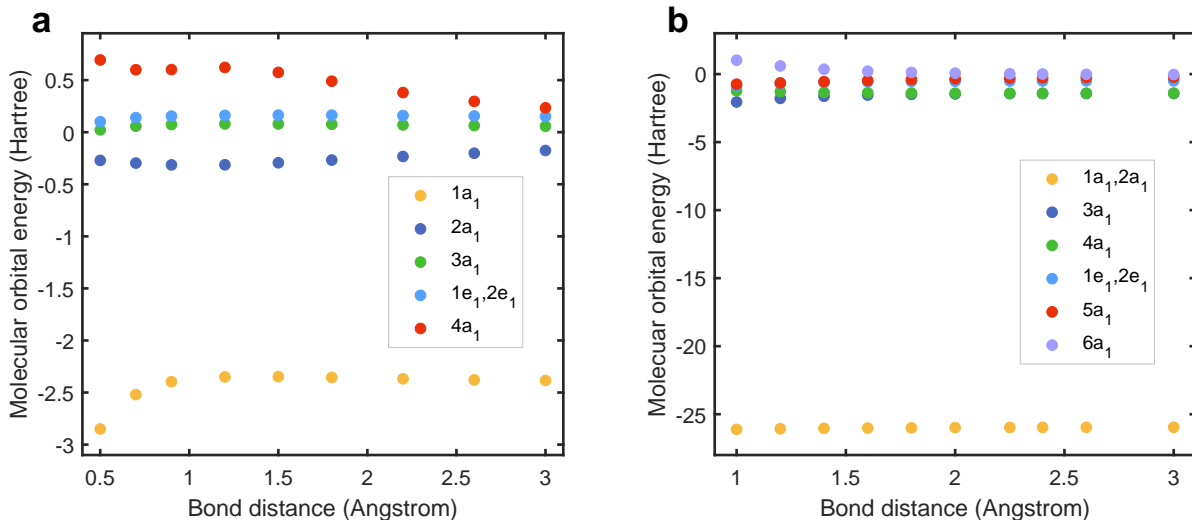


FIG. 9. Hartree Fock orbital energies for the (a) LiH and (b) F₂ molecules. Each Hartree Fock is represented by a coloured node in the figure, indexed by its irrep. Molecular orbitals with close energy are combined.

as only closed-shell molecules are considered, the reference state is restricted to a singlet state. In the first step of generating the molecular Hamiltonians, we adopt the restricted Hartree-Fock (RHF) method, where the ground-state wave function Ψ_0 is expressed by a single Slater determinant of molecular orbitals. The energy $E = \langle \Psi_0 | H | \Psi_0 \rangle$ is then minimised subject to orbital orthogonality. We first consider the initial state to be a single reference state (i.e., a product state in the computational basis). Suppose the total number of electrons is 2η . The single reference state is constructed in a way that η of electrons occupy the lowest energy spin orbitals in the spin α and β sectors, respectively, which is referred to as the Hartree-Fock state $|\Psi_{\text{HF}}\rangle$.

In this work, qubits are arranged in the following way: i) From left to right, each qubit corresponds to a spin-orbital that increases in its molecular-orbital energy; ii) The spin α and β sector are arranged separately; the spin α is assigned first in the left part, then followed by the spin β part. For example, the HF state of the 6-qubit, 2-electron LiH molecule reads $|100100\rangle$, where the first and last 3-qubit state $|100\rangle$ correspond to the spin α and β parts, respectively.

Conventionally, the HF state is a good initial guess when the molecule is close to equilibrium. However, the closer the molecule approaches dissociation, the worse the HF state behaves due to the quasi-degeneration of different configurations. Consequently, the correlation energy, defined as the difference between the ground state energy and HF energy, becomes larger when the bond distance of a bi-atomic molecule stretches. To address this point, we consider the reference state to be a superposition of multi-configurations,

$$|\Psi_{\text{ref}}\rangle = \sum_i c_i |\Psi_i\rangle, \quad (5)$$

where $\{|\Psi_i\rangle\}$ is the collection of configurations in the reference state with coefficients $\{c_i\}$. The configurations $|\Psi_i\rangle$ are chosen by identifying the fermionic modes that are related to the bond-breaking process and the size $|\{|\Psi_i\rangle\}|$ is a constant as they are only related to a constant number of fermionic modes. Thus, we can optimise efficiently on a classical device to determine the optimal coefficients. This approach is known as a multi-reference method [6] in the quantum chemistry literature. We apply the method for the LiH and F₂ molecule and observe that higher accuracy is achieved compared to the HF state in the dissociation regime. As the two molecules we considered here are bi-atomic, the molecule can be seen as two individual atoms with negligible interaction in the large bond-distance limit. Also, the molecular orbitals are constructed as a linear combination of atomic orbitals in a symmetry-adapted way such that two atomic orbitals with the same symmetry are combined in a linear way to two molecular orbitals. For the LiH molecule, the lowest two molecular orbitals in the active space are established from atomic orbitals in this way. Hence, in the dissociation limit, one decouples the molecular orbitals to atomic ones by the equal-superposition state $\frac{1}{\sqrt{2}}|100100\rangle - \frac{1}{\sqrt{2}}|010010\rangle$ where the other configuration is selected as $|010010\rangle$ for the reference. The same logic follows for other molecules. As the molecule is in the intermediate state that interpolates between the equilibrium

and the dissociation regimes, it is expected the reference state to be a superposition of the above-mentioned two configurations. We elaborate on the compilation of quantum circuits and optimise the coefficients of the reference state in the following.

In this work, we prepare the reference state as

$$|\Psi_{\text{ref}}\rangle = \frac{1}{\sqrt{1+\beta^2}}(1 - \beta \hat{a}_{\eta+N/2}^\dagger \hat{a}_\eta^\dagger \hat{a}_{\eta+N/2-1} \hat{a}_{\eta-1}) |\Psi_{\text{HF}}\rangle, \quad (6)$$

which considers the excitations from the highest occupied molecular orbitals of the Hartree-Fock state, and the qubits are numbered from 0. When $\beta = 0$, the initial state reduces to the Hartree-Fock state. The quantum circuit for preparing the multi-reference state in Eq. (6) is first creating a rotation along the y-axis on the qubit indexed by $(\eta - 1)$ as

$$R_y |0\rangle^{\otimes N} = \frac{1}{\sqrt{1+\beta^2}} |0\rangle^{\otimes(\eta-1)} \otimes (|0\rangle - \beta |1\rangle) \otimes |0\rangle^{\otimes N-\eta}, \quad (7)$$

followed by 3 CNOT gates and single-qubit X gates, which can be explicitly expressed as

$$\left(\begin{array}{cc} \bigotimes_{i=N/2}^{\eta+N/2-1} & \bigotimes_{i=0}^{\eta-1} \\ X_i & X_i \end{array} \right) \text{CNOT}_{(N/2+\eta-1) \rightarrow (N/2+\eta)} \text{CNOT}_{\eta \rightarrow (N/2+\eta-1)} \text{CNOT}_{(\eta-1) \rightarrow \eta}. \quad (8)$$

It is easy to find that compared to the Hartree-Fock state, the state preparation for Eq. (6) only introduces additional 3 CNOT gates. For instance, we prepare $|\Psi_0\rangle = \frac{1}{\sqrt{1+\beta^2}}(|100100\rangle - \beta |010010\rangle)$ for the LiH molecule. The circuit for initial state preparation is shown in Fig. 10.

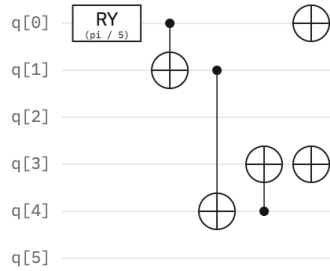


FIG. 10. The initial state preparation for LiH molecule $|\Psi_0\rangle = \frac{1}{\sqrt{1+\beta^2}}(|100100\rangle - \beta |010010\rangle)$. The Pauli rotation along the y-axis prepares the state $R_y |0\rangle = \frac{1}{\sqrt{1+\beta^2}}(|0\rangle - \beta |1\rangle)$.

The parameter β is determined by minimising the energy on the state, i.e., $\min_\beta \langle \Psi_0 | \hat{H} | \Psi_0 \rangle$. It is easy to check that this minimisation problem can be computed efficiently.

A comparison of the initial state energy associated with the multi-reference state, Hartree-Fock state energy, and the true ground state energy is shown in Fig. 11. The multi-reference state outperforms the Hartree-Fock state at a large bond distance and thus serves as a better initial state in this case.

C. Quantum circuit ansatz design and compilation

1. Unitary coupled cluster circuit ansatz

One crucial step for simulating large molecular systems by variational quantum algorithms is to design an appropriate quantum circuit that can effectively represent the ground state of the target system, and meanwhile, circuit depth is shallow. The unitary coupled cluster (UCC) ansatz has been widely used in the context of quantum computational chemistry [37]. As shown in the main text, the quantum state can be constructed as

$$|\Psi(\boldsymbol{\theta})\rangle = e^{\hat{T}(\boldsymbol{\theta}) - \hat{T}^\dagger(\boldsymbol{\theta})} |\Psi_0\rangle, \quad (9)$$

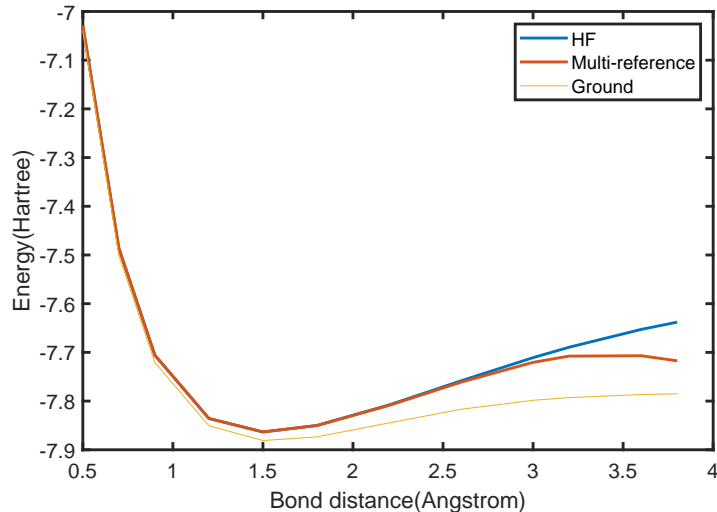


FIG. 11. Comparison of different energies associated with the Hartree-Fock state, the multi-reference state, and the ground state.

where $\hat{T}(\boldsymbol{\theta})$ is the coupled-cluster excitations, and $|\Psi_0\rangle$ is the initial state. The coupled-cluster excitations are usually truncated to single and double excitations, which are also called unitary coupled-cluster singles-and-doubles (UCCSD). The cluster operator truncated at single- and double-excitations has the form

$$\hat{T}(\boldsymbol{\theta}) = \sum_{\substack{p \in \text{vir} \\ i \in \text{occ}}} \theta_{pi} \hat{T}_{pi} + \sum_{\substack{p, q \in \text{vir} \\ i, j \in \text{occ}}} \theta_{pqji} \hat{T}_{pqji}, \quad (10)$$

where the one- and two-body terms are defined as $\hat{T}_{pi} = \hat{a}_p^\dagger \hat{a}_i$ and $\hat{T}_{pqji} = \hat{a}_p^\dagger \hat{a}_q^\dagger \hat{a}_j \hat{a}_i$, respectively. As the molecular Hamiltonian conserves particles with definite spins, the ansatz is designed to conserve this symmetry as well, whereas the spin degree of freedom is abbreviated for simplicity.

To implement the VQE circuit of UCC ansatz on a quantum device, we apply the first-order Trotter-Suzuki expansion. and the circuit ansatz becomes

$$|\Psi(\boldsymbol{\theta})\rangle = \prod_{\hat{T}_i \in \mathcal{O}} e^{\hat{T}_i - \hat{T}_i^\dagger} |\Psi_0\rangle, \quad (11)$$

where we denote the operator pool as $\mathcal{O} := \{\hat{T}_i\}$ with \hat{T}_i representing the excitation operators in Eq. (10). Here, it is worth remarking that the order of \hat{T}_i will result in a different performance of the circuit.

As can be found from Eq. (10) and Eq. (11), the original UCCSD ansatz considering the single- and double-excitations is composed of a large number of operators scaling as $\mathcal{O}((N - \eta)^2 \eta^2)$ with electron number η , and the circuit depth with respect to the two-qubit entangling gates scales as $\mathcal{O}(N(N - \eta)^2 \eta^2)$. As shown in the main text, the CZ gate counts for H_2 , LiH , and F_2 are 56, 280, 2920, respectively. Note that the multi-qubit rotation gate is compiled into a ladder of CZ gates and a single-qubit Pauli rotation gate, $\exp(-i\theta \hat{\sigma}/2)$, with $\hat{\sigma} = \{X, Y, Z\}$ being the single-qubit Pauli operator. The high demand for the CZ gates constraints practical implementation of the original UCC ansatz.

2. Point group symmetry constraint

There has been considerable progress in reducing the number of operators in the circuit ansatz, such as using classical pre-calculation to screen out the terms that are small enough [35] or only choosing the important excitation operators [58], for instance, paired double excitation operators in ansatz [59]. In the following, we discuss the circuit reduction strategy using the point group symmetry constraint.

To reduce the circuit depth without sacrificing accuracy, we consider using the point group property to reduce the UCC ansatz operators. Point group symmetry (spatial symmetry) is a fundamental property of molecular systems that

characterises molecules' geometric and electronic structures. The amplitude associated with the one- and two-electron excitations in both coupled cluster and unitary coupled cluster ansatz is proven to be zero unless the corresponding term preserves the symmetry of the initial state [38]. This indicates that the expansion of the unitary coupled cluster wavefunction will only contain the terms with the same irreducible representation (irrep) as the reference wavefunction [39]. For the simple closed-shell molecules, the excitation operations should preserve the symmetry, and thus the irrep of the ground state should be A_g , which is a totally symmetric irreducible representation, A_g , of which the characters are all 1. This applies to all the cases considered in this work.

In our implementation, we filter out the operators that break the symmetry of the reference Hartree-Fock state when constructing the UCC ansatz. Only the terms excite $|\Psi_0\rangle$ to A_g states remain, and the rest of the terms in the exciting operator are excluded in constructing the cluster operator. As such, we select the operators \hat{T}_i that satisfy the constraint of symmetry, that is,

$$\mathcal{O} := \left\{ \hat{T}_i \mid D \left(e^{\hat{T}_i - \hat{T}_i^\dagger} |\Psi_0\rangle \right) = D(|\Psi_0\rangle) \right\} \quad (12)$$

where D is the irrep of the corresponding wavefunction.

The point group of LiH is $C_{\infty v}$, which has three irreducible representations D , i.e. $D \in \{A_g, E_{1x}, E_{1y}\}$. All the UCCSD excitation operators satisfy the symmetry constraint in Eq. (12), and thus there is no circuit reduction for LiH. However, for large molecules, quantum circuits can be reduced without sacrificing accuracy. The point group of F_2 is $D_{\infty h}$. F_2 has six irreducible representations D , $D \in \{A_{1g}, E_{1gx}, E_{1gy}, A_{1u}, E_{1uy}, E_{1ux}\}$. In total, there are ten single excitation operators and 25 double excitation operators. Only nine excitations have the same irreducible representation of A_{1g} and need to be included in the circuit ansatz.

However, we note that the strategy based on Point group symmetry constraints may not yield significant reductions in circuit depth for larger molecules which tend to be less symmetric. Below, we introduce a circuit reduction strategy by selecting the dominant excitation operations.

3. Selection of excitation operators

The above circuit reduction exploits intrinsic information of the molecules. We can further construct a more compact quantum circuit by selecting operators that contribute dominantly to the energy decrease from a reference state, which has been proposed in [40]. We start from the initial state $|\Psi_0\rangle$, which is a Hartree-Fock state or a multi-reference state. The excitation operators are selected from the UCCSD operator pool \mathcal{O} in Eq. (10) composed of the possible single- and double-excitation operators \hat{T}_{pi} and \hat{T}_{pqji} that satisfy the symmetry constraints.

This relies on the fact that the quantum circuit with a single operator can be efficiently simulated. The quantum state under one excitation becomes

$$|\Psi\rangle = e^{\theta(\hat{T}_i - \hat{T}_i^\dagger)} |\Psi_0\rangle, \quad (13)$$

where $\hat{T}_i \in \mathcal{O}$ is a one-body or two-body excitation operator in the operator pool \mathcal{O} with the form $\hat{T}_i = \hat{a}_p^\dagger \hat{a}_i$ or $\hat{a}_p^\dagger \hat{a}_q^\dagger \hat{a}_j \hat{a}_i$. The VQE optimisation iteration is carried for each operator $\hat{T}_i \in \mathcal{O}$ for E_i . The minimised energy is obtained by the variational principle

$$E_i = \min_{\theta_i} \langle \Psi_0 | e^{-\theta_i(\hat{T}_i - \hat{T}_i^\dagger)} \hat{H} e^{\theta_i(\hat{T}_i - \hat{T}_i^\dagger)} | \Psi_0 \rangle. \quad (14)$$

The importance of the operator is evaluated by calculating the energy difference with respect to the initial state energy, $\Delta E_i = |E_0 - E_i|$, with $E_0 = \langle \Psi_0 | \hat{H} | \Psi_0 \rangle$. The list $\{(\Delta E_i, \hat{T}_i)\}_{\text{sorted}}$ is recorded. The operators are sorted according to the energy difference in descending order. The operators with contributions above a threshold $|\Delta E_i| > \varepsilon_{\text{thres}}$ are picked out and used to perform the VQE optimisation. In what follows, we show that this selection procedure is classically efficient.

The circuit operator $e^{\theta(\hat{T}_i - \hat{T}_i^\dagger)}$ can be expanded by the Taylor series as

$$\begin{aligned} e^{\theta(\hat{T}_i - \hat{T}_i^\dagger)} &= \sum_{n=0}^{\infty} \frac{\theta^n (\hat{T}_i - \hat{T}_i^\dagger)^n}{n!} \\ &= I + \sum_{n=1}^{\infty} (-1)^n \theta^{2n} \frac{(\hat{T}_i \hat{T}_i^\dagger)^n + (\hat{T}_i^\dagger \hat{T}_i)^n}{(2n)!} + \sum_{n=0}^{\infty} (-1)^n \theta^{2n+1} \frac{-\hat{T}_i^\dagger (\hat{T}_i \hat{T}_i^\dagger)^n + \hat{T}_i (\hat{T}_i^\dagger \hat{T}_i)^n}{(2n+1)!} \\ &= \cos(\theta \sqrt{\hat{T}_i \hat{T}_i^\dagger}) + \cos(\theta \sqrt{\hat{T}_i^\dagger \hat{T}_i}) - \frac{\hat{T}_i^\dagger}{\sqrt{\hat{T}_i \hat{T}_i^\dagger}} \sin(\theta \sqrt{\hat{T}_i \hat{T}_i^\dagger}) + \frac{\hat{T}_i}{\sqrt{\hat{T}_i^\dagger \hat{T}_i}} \sin(\theta \sqrt{\hat{T}_i^\dagger \hat{T}_i}) \end{aligned} \quad (15)$$

where we have used $\hat{T}_i^2 = (\hat{T}_i^\dagger)^2 = 0$. From Eq. (15), the circuit operator comprises four terms only, and each term can be simulated classically [60]. Let us take $\cos(\theta\sqrt{\hat{T}_i\hat{T}_i^\dagger})$ for example. Without loss of generality, \hat{T}_i can be expressed as $\hat{T}_i = \hat{a}_3^\dagger\hat{a}_1^\dagger\hat{a}_2\hat{a}_0$, and then

$$\hat{T}_i\hat{T}_i^\dagger = \hat{a}_3^\dagger\hat{a}_1^\dagger\hat{a}_2\hat{a}_0\hat{a}_0^\dagger\hat{a}_2^\dagger\hat{a}_1\hat{a}_3 = \hat{n}_3\hat{n}_1(1-\hat{n}_2)(1-\hat{n}_0). \quad (16)$$

Since the action of the number operator gives 0 or 1 and $\hat{T}_i\hat{T}_i^\dagger$ is idempotent, the square root of $\hat{T}_i\hat{T}_i^\dagger$ can be defined as

$$\sqrt{\hat{T}_i\hat{T}_i^\dagger} \equiv \hat{n}_3\hat{n}_1(1-\hat{n}_2)(1-\hat{n}_0), \quad (17)$$

and we have

$$\cos(\theta\sqrt{\hat{T}_i\hat{T}_i^\dagger}) = \cos\theta\sqrt{\hat{T}_i\hat{T}_i^\dagger} = \cos\theta\hat{n}_3\hat{n}_1(1-\hat{n}_2)(1-\hat{n}_0). \quad (18)$$

The energy expectation $\langle\Psi_0|e^{-\theta(\hat{T}_i-\hat{T}_i^\dagger)}\hat{H}e^{\theta(\hat{T}_i-\hat{T}_i^\dagger)}|\Psi_0\rangle$ contains 16 terms, each of which can be simulated classically. Therefore, the optimisation process described by Eq. (14) can be simulated classically.

The above discussion holds for any operators, and hence their actions on any states. The expression can be further simplified when we consider the action of the operator on the Hartree-Fock state. Define $\hat{G} := -i(\hat{T}_i - \hat{T}_i^\dagger)$. It is easy to check that G is Hermitian $\hat{G} = G^\dagger$. For T contains only one excitation, the action of G on the HF state $|\Psi_{\text{HF}}\rangle$ is

$$\hat{G}^2|\Psi_{\text{HF}}\rangle = -(\hat{T}_i^2 + (\hat{T}_i^\dagger)^2 - \hat{T}_i\hat{T}_i^\dagger - \hat{T}_i^\dagger\hat{T}_i)|\Psi_{\text{HF}}\rangle = |\Psi_{\text{HF}}\rangle. \quad (19)$$

Therefore, we have

$$|\Psi\rangle = e^{i\theta\hat{G}}|\Psi_{\text{HF}}\rangle = (\cos\theta\hat{I} + i\sin\theta\hat{G})|\Psi_{\text{HF}}\rangle. \quad (20)$$

The energy can now be calculated as

$$\langle\Psi_{\text{HF}}|e^{-\theta(\hat{T}_i-\hat{T}_i^\dagger)}\hat{H}e^{\theta(\hat{T}_i-\hat{T}_i^\dagger)}|\Psi_{\text{HF}}\rangle = E_0\cos^2\theta + \sin^2\theta\langle\Psi_{\text{HF}}|\hat{G}\hat{H}\hat{G}|\Psi_{\text{HF}}\rangle \quad (21)$$

with $E_0 = \langle\Psi_{\text{HF}}|\hat{H}|\Psi_{\text{HF}}\rangle$. It is straightforward to see that this optimisation process with one excitation operator acting on the Hartree-Fock state can be simulated classically.

Suppose we have selected the operator set $\{\hat{T}_i\}$ in its qubit form. We map \hat{T}_i to its qubit form under the Jordan-Wigner transformation. Since each term is symmetric and the contribution of each term is the same, we only choose one term in the qubit form to further reduce the gate count and hence circuit depth. In the next section, we display the quantum circuits for the three molecules.

4. Quantum circuit compilation

In this section, we present the dominant operators and quantum circuits for the three molecules after circuit compilation. The dominant excitation operators for H_2 are $a_3^\dagger a_1^\dagger a_2 a_0$. The dominant excitation operators for LiH are $a_5^\dagger a_1^\dagger a_3 a_0$, $a_4^\dagger a_2^\dagger a_3 a_0$, and $a_5^\dagger a_2^\dagger a_3 a_0$. The dominant excitation operators for F_2 are $a_{11}^\dagger a_5^\dagger a_6 a_0$, $a_{11}^\dagger a_5^\dagger a_7 a_1$, $a_{11}^\dagger a_5^\dagger a_8 a_2$, $a_{11}^\dagger a_5^\dagger a_9 a_3$, and $a_{11}^\dagger a_5^\dagger a_{10} a_4$.

Next, we optimise the quantum circuits with respect to the circuit depth of CZ gates. We exploit the 2D geometry of the qubit layout of the quantum processor to encode the spin-ups and spin-downs, and we optimise the depth by parallelisation of CZ gates. The parameterised quantum circuits for H_2 , LiH and F_2 are

$$U_{\text{H}_2} = \exp(i\theta X_0 Y_1 X_2 X_3) \exp(-i\theta Y_0 X_1 X_2 X_3), \quad (22)$$

$$U_{\text{LiH}} = \exp(-i\theta_3 Y_0 Z_1 X_2 X_3 Z_4 X_5) \exp(-i\theta_2 Y_0 Z_1 X_2 X_3 X_4) \exp(-i\theta_1 Y_0 X_1 X_3 Z_4 X_5), \quad (23)$$

and

$$U_{\text{F}_2} = \exp(-i\theta_5 X_4 X_5 Y_{10} X_{11}) \exp(-i\theta_4 Y_3 Z_4 X_5 X_9 Z_{10} X_{11}) \exp(-i\theta_3 Y_2 Z_3 Z_4 X_5 X_8 Z_9 Z_{10} X_{11}) \\ \exp(-i\theta_2 Y_1 Z_2 Z_3 Z_4 X_5 X_7 Z_8 Z_9 Z_{10} X_{11}) \exp(-i\theta_1 Y_0 Z_1 Z_2 Z_3 Z_4 X_5 X_6 Z_7 Z_8 Z_9 Z_{10} X_{11}), \quad (24)$$

respectively.

The compiled quantum circuits (excluding the initial state preparation and measurement) for H_2 , LiH , and F_2 are shown in Fig. 12, Fig. 13, and Fig. 14, respectively. Here, the parameters are chosen as $\pm\pi/5$ as an example. The circuit for initial preparation has been discussed in Sec. II B, and the circuit for LiH is shown in Fig. 10.

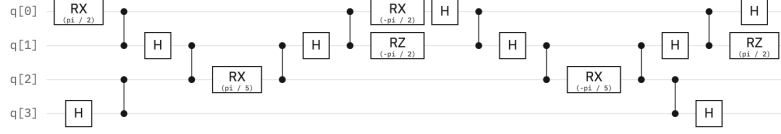
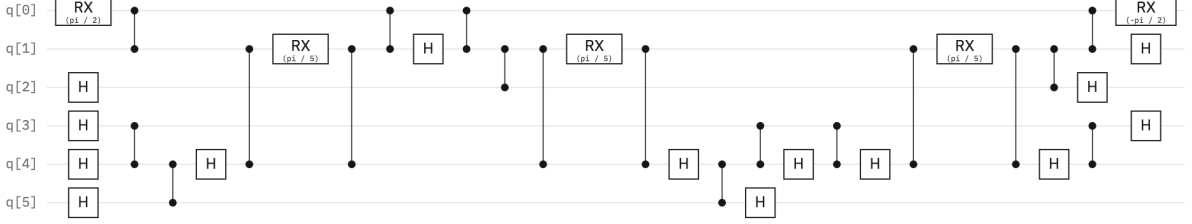
FIG. 12. The compiled quantum circuit ansatz for H₂.

FIG. 13. The compiled quantum circuit ansatz for LiH

D. Optimisation by analytic stochastic gradient descent

Now, we show how to analytically estimate the gradient of expectation values of the observable \hat{O} . In VQE, the ground state is approximated by solving $\mathcal{L}(\boldsymbol{\theta}) = \min_{\boldsymbol{\theta}} \langle \Psi_0 | U^\dagger(\boldsymbol{\theta}) \hat{O} U(\boldsymbol{\theta}) | \Psi_0 \rangle_{\boldsymbol{\theta}}$ with $\hat{O} = \hat{H}$ using a classical optimiser. The circuit that is constructed using the methods developed in Sec. II C takes the form of

$$U(\boldsymbol{\theta}) = \prod_j \prod_{l_j} V_{j,l_j}(\boldsymbol{\theta}_j), \quad (25)$$

where each gate operation V_{j,l_j} is a multi-qubit Pauli rotation $V_{j,l_j} = \exp(-i\boldsymbol{\theta}_j P_{j,l_j}/2)$ with $P_{j,l_j} \in \{I, X, Y, Z\}^{\otimes N}$ being the tensor product of single-qubit Pauli operators over N qubits. Prior works usually consider $L_j = 1$, that is, each parameter is associated with only one term. However, in quantum chemistry experiments, the parameters are often associated with many terms. The objective is to get the first-order derivative with respect to the j th parameter, i.e., $g_j(\boldsymbol{\theta}) = \partial \mathcal{L}(\boldsymbol{\theta}) / \partial \boldsymbol{\theta}_j$. Using the Leibniz rule, the gradient is given by

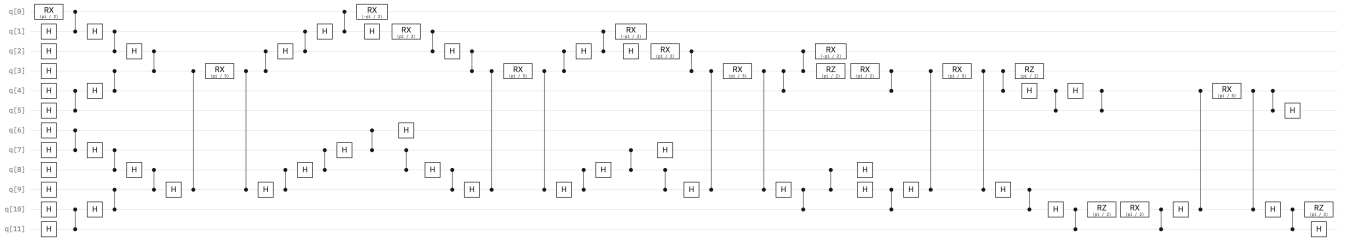
$$g_j = \sum_{l_j} \langle \Phi_{j,l_j} | \frac{\partial \bar{V}_{j,l_j}(\boldsymbol{\theta}_{j,l_j})}{\partial \boldsymbol{\theta}_{j,l_j}} | \Phi_{j,l_j} \rangle \quad (26)$$

where we introduce $\boldsymbol{\theta}_{j,l_j}$ to represent the parameter associated with the operator V_{j,l_j} with $\boldsymbol{\theta}_{j,l_j} = \boldsymbol{\theta}_j$, and we have

$$|\Phi_{j,l_j}\rangle = \prod_{k < l_j} V_{j,k}(\boldsymbol{\theta}_{j,k}) \prod_{k < j} \prod_{l_k} V_{k,l_k}(\boldsymbol{\theta}_{k,l_k}) |\Psi_0\rangle \quad (27)$$

and

$$\bar{V}_{j,l_j}(\boldsymbol{\theta}_{j,l_j}) = V_{j,l_j}(\boldsymbol{\theta}_{j,l_j})^\dagger \bar{O} V_{j,l_j}(\boldsymbol{\theta}_{j,l_j}) \quad (28)$$

FIG. 14. The compiled quantum circuit ansatz for F₂

with

$$\bar{O} = \left(\prod_{k>j} \prod_{l_k} V_{k,l_k}(\boldsymbol{\theta}_{k,l_k}) \prod_{k>l_j} V_{j,k}(\boldsymbol{\theta}_{j,k}) \right)^\dagger O \prod_{k>j} \prod_{l_k} V_{k,l_k}(\boldsymbol{\theta}_{k,l_k}) \prod_{k>l_j} V_{j,k}(\boldsymbol{\theta}_{j,k}). \quad (29)$$

Since $P_{j,l_j}^2 = I$, each of the gate can be written as

$$V_{j,l_j}(\boldsymbol{\theta}_{j,l_j}) = \cos(\boldsymbol{\theta}_{j,l_j}/2)I - i \sin(\boldsymbol{\theta}_{j,l_j}/2)P_{j,l_j}, \quad (30)$$

and thus $\bar{V}_{j,l_j}(\boldsymbol{\theta}_{j,l_j})$ can be written as

$$\bar{V}_{j,l_j}(\boldsymbol{\theta}_{j,l_j}) = A + B \cos(\boldsymbol{\theta}_{j,l_j}) + C \sin(\boldsymbol{\theta}_{j,l_j}) \quad (31)$$

where A , B , and C are operators that rely on V_{j,l_j} and \bar{O} yet independent of the parameters $\boldsymbol{\theta}_{j,l_j}$. From Eq. (31), we can show that the summand in the gradient is related to a parameter-shifted $\bar{V}_{j,l_j}(\boldsymbol{\theta}_{j,l_j} \pm s)$ with a shift s , which is given by

$$\frac{\partial \bar{V}_{j,l_j}(\boldsymbol{\theta}_{j,l_j})}{\boldsymbol{\theta}_{j,l_j}} = \frac{\bar{V}_{j,l_j}(\boldsymbol{\theta}_{j,l_j} + s) - \bar{V}_{j,l_j}(\boldsymbol{\theta}_{j,l_j} - s)}{2 \sin s}. \quad (32)$$

The gradient is thus given by

$$\begin{aligned} g_j &= \frac{\sum_{l_j} (\langle \Phi_{j,l_j} | \bar{V}_{j,l_j}(\boldsymbol{\theta} + s \mathbf{e}_{j,l_j}) | \Phi_{j,l_j} \rangle - \langle \Phi_{j,l_j} | \bar{V}_{j,l_j}(\boldsymbol{\theta} - s \mathbf{e}_{j,l_j}) | \Phi_{j,l_j} \rangle)}{2 \sin(s)} \\ &= \frac{\sum_{l_j} \mathcal{L}(\boldsymbol{\theta} + s \mathbf{e}_{j,l_j}) - \mathcal{L}(\boldsymbol{\theta} - s \mathbf{e}_{j,l_j})}{2 \sin(s)} \end{aligned} \quad (33)$$

with unit vector \mathbf{e} . Eq. (33) indicates that we can get the gradient of the energy expectation analytically by measuring the energy expectation by shifting parameters, termed the parameter-shift rule [61, 62].

In the experiment, the gradient is estimated by measuring the two parameter-shifted quantities. Due to statistical fluctuation, the gradient can only be estimated up to certain precision. The estimator of g_j is given by

$$\hat{g}_j = \frac{\sum_{l_j} \hat{\mathcal{L}}(\boldsymbol{\theta} + s \mathbf{e}_{j,l_j}) - \hat{\mathcal{L}}(\boldsymbol{\theta} - s \mathbf{e}_{j,l_j})}{2 \sin(s)}. \quad (34)$$

The estimation by the parameter-shift rule has an unbiased estimation of the gradient as

$$\mathbb{E} \hat{g}_j = g_j. \quad (35)$$

In what follows, we discuss the variance of the estimator. Assume that energy estimation has the same variance as

$$\text{Var}[\hat{\mathcal{L}}] = \text{Var}[\hat{\mathcal{L}}(\boldsymbol{\theta} + s \mathbf{e}_{j,l_j})], \quad \forall j, \forall l_j. \quad (36)$$

Then the variance of the gradient estimation is given by

$$\text{Var}[\hat{g}_j] = \frac{L_j}{\sin^2(s)} \text{Var}[\hat{\mathcal{L}}] \geq L_j \text{Var}[\hat{\mathcal{L}}]. \quad (37)$$

It is straightforward that the variance of the estimator is minimised when $s = \pi/2$.

The gradient estimation by the parameter-shift rule shows a clear advantage over the finite difference method where the gradient is estimated as

$$\hat{g}_j^{\text{FD}} = \frac{\sum_{l_j} \hat{\mathcal{L}}(\boldsymbol{\theta} + \delta \mathbf{e}_{j,l_j}) - \hat{\mathcal{L}}(\boldsymbol{\theta} - \delta \mathbf{e}_{j,l_j})}{2\delta}. \quad (38)$$

The estimation is unbiased when the step size approaches zero, $\delta \rightarrow 0$. To make the estimation close to the true gradient, the step δ should be taken to be a small number. However, the variance of the estimation is

$$\text{Var}[\hat{g}_j^{\text{FD}}] = \frac{L_j}{\delta^2} \text{Var}[\hat{\mathcal{L}}], \quad (39)$$

which can be much larger than the variance in Eq. (37).

To make it more efficient, we adopt a stochastic gradient descent strategy. For the k th iteration with parameters $\boldsymbol{\theta}^k$, we obtain the gradient element $g_j^k(\boldsymbol{\theta}^k)$ by the parameter shift rule

$$\hat{g}_j^{\text{SGD},k}(\boldsymbol{\theta}^k) = \frac{\hat{\mathcal{L}}(\boldsymbol{\theta}^+) - \hat{\mathcal{L}}(\boldsymbol{\theta}^-)}{2} \quad (40)$$

where we define

$$\hat{\mathcal{L}}(\boldsymbol{\theta}^\pm) = \sum_{l_j} \hat{\mathcal{L}}(\boldsymbol{\theta} \pm \pi \Delta_j \mathbf{e}_{j,l_j}/2). \quad (41)$$

In experiments, the parameters to be optimised are chosen stochastically by $\Delta_j^k = 0$ or 1 and satisfying $|\Delta^k| > N_p/2$ to reduce the sample cost for the gradients. We update the parameters by $\boldsymbol{\theta}^{k+1} = \boldsymbol{\theta}^k + \alpha^k \mathbf{g}^k(\boldsymbol{\theta}^k)$ with an appropriate learning rate α^k . The estimation of the gradient is also unbiased

$$\mathbb{E} \hat{g}_j^{\text{SGD},k}(\boldsymbol{\theta}^k) = g_j^k(\boldsymbol{\theta}^k). \quad (42)$$

E. Quantum state measurement and classical post-processing

The power of variational quantum algorithms is at the expense of measurements. This becomes a severe problem in molecular systems, in which the number of measurements at each iteration scales up to $\mathcal{O}(N^4)$ with the problem size N . However, as many of the observables have small coefficients and are qubit-wise compatible (hence could be measured simultaneously), we could exploit more efficient measurement schemes to alleviate the measurement cost. In this section, we discuss how to measure the observable efficiently by exploiting the qubit-wise compatibility of the target observable.

1. Overlapped grouping measurement

The observables in our experiment include the Hamiltonian \hat{H} , the projected Hamiltonian in the symmetry verified space $\Pi \hat{H} \Pi$ with the projector Π , and Hamiltonian moments \hat{H}^k for $k \geq 2$. The target observable \mathbf{O} can be decomposed into the Pauli basis as

$$\mathbf{O} = \sum_l \alpha_l \mathbf{O}_l, \quad (43)$$

with $\mathbf{O}_l \in \{I, X, Y, Z\}^{\otimes n}$ being the tensor product of single-qubit Pauli operators. The main idea is that if two observables \mathbf{O}_l and $\mathbf{O}_{l'}$ are qubit-wise compatible, we can measure the two observables simultaneously in one measurement basis. Formally, for a multi-qubit Pauli operator $\mathbf{Q} = \otimes_{i=1}^n Q_i$ with $Q_i \in \{I, X, Y, Z\}$ being a single-qubit Pauli operator acting on the i th qubit, its expectation value can be obtained by measurements in any Pauli basis $\mathbf{P} = \otimes_{i=1}^n P_i$ whenever $Q_i = P_i$ or $Q_i = I$ for any i . We refer to this circumstance as \mathbf{P} hits \mathbf{Q} and denote by $\mathbf{Q} \triangleright \mathbf{P}$. We say that \mathbf{O}_l and $\mathbf{O}_{l'}$ are compatible with each other when $\mathbf{O}_l \triangleright \mathbf{P}$ and $\mathbf{O}_{l'} \triangleright \mathbf{P}$, i.e., they are hit by the same basis \mathbf{P} .

To estimate $\text{Tr}(\rho \mathbf{O})$ for an n -qubit unknown quantum state ρ , we randomly select the measurement basis \mathbf{P} and generate an estimation of $\text{Tr}(\rho \mathbf{O})$ by measuring in the measurement basis \mathbf{P} with probability $\mathcal{K}(\mathbf{P})$. An estimator of the target observable \mathbf{O} is expressed as

$$\hat{\mathbf{o}}(\mathbf{P}) = \sum_l \alpha_l f(\mathbf{P}, \mathbf{O}_l, \mathcal{K}) \mu(\mathbf{P}, \text{supp}(\mathbf{O}_l)) \quad (44)$$

where $\mu(\mathbf{P}, \text{supp}(\mathbf{O}_l)) = \prod_{i \in \text{supp}(\mathbf{O}_l)} \mu(P_i)$ with $\mu(P_i)$ being the single-shot outcome of measurement P_i on the i th qubit, $\text{supp}(\mathbf{Q}) = \{i | Q_i \neq I\}$. Suppose we have chosen the measurement basis set $\{\mathbf{P}_j\}$ and the associated probability distribution $\{\mathcal{K}(\mathbf{P}_j)\}$, the function f is defined as

$$f(\mathbf{P}, \mathbf{Q}, \mathcal{K}) = \chi(\mathbf{Q})^{-1} \delta_{\mathbf{Q} \triangleright \mathbf{P}}, \quad (45)$$

where $\chi(\mathbf{Q}) = \sum_{\mathbf{P}: \mathbf{Q} \triangleright \mathbf{P}} \mathcal{K}(\mathbf{P})$ represents the probability that \mathbf{Q} is effectively measured with the measurement basis \mathbf{P} . Eq. (44) gives an unbiased estimation

$$\mathbb{E}[\hat{\mathbf{o}}] = \text{Tr}(\mathbf{O}\rho), \quad (46)$$

where the average is over the probability distribution $\mathcal{K}(\mathbf{P})$. The variance of the estimator in Eq. (44) for a single sample could be calculated by the definition as

$$\text{Var}[\hat{\mathbf{o}}] = \mathbb{E}_{\mathbf{P}} \sum_{l,l'} \alpha_l \alpha_{l'} \text{Tr}(\rho \mathbf{O}_l \mathbf{O}_{l'}) f(\mathbf{P}, \mathbf{O}_l, \mathcal{K}) f(\mathbf{P}, \mathbf{O}_{l'}, \mathcal{K}) - \text{Tr}(\rho \mathbf{O})^2, \quad (47)$$

where we use the equality $\mathbb{E}_{\mu(\mathbf{P})} \mu(\mathbf{P}, \text{supp}(\mathbf{O}_l)) \mu(\mathbf{P}, \text{supp}(\mathbf{O}_{l'})) = \mathbb{E}_{\mu(\mathbf{P})} \mu(\mathbf{P}, \text{supp}(\mathbf{O}_l \mathbf{O}_{l'})) = \text{Tr}(\rho \mathbf{O}_l \mathbf{O}_{l'})$. The detailed proof can be found in Refs. [43, 63].

We assign the observables $\{\mathbf{O}_l\}$ into overlapped grouping sets,

$$\mathcal{S} = \{\mathbf{e}_1, \dots, \mathbf{e}_s\}, \quad (48)$$

where each set \mathbf{e}_j is composed of compatible observables that can be measured in basis \mathbf{P}_j and it satisfies

$$\cup_j \mathbf{e}_j = \mathcal{O}, \quad \mathbf{e}_j = \{\mathbf{Q} \triangleright \mathbf{P}_j\}, \quad \forall \mathbf{Q} \in \mathbf{e}_j. \quad (49)$$

The strategy to determine the overlapped grouping sets is that we add an observable \mathbf{O}_l that has not been accessed into a new set and all compatible observables into this set. Observables with larger absolute weights are given high priority since they have more contributions to the variance, as can be found from Eq. (47). The algorithm generates the measurements $\{\mathbf{P}\}$ with non-optimised probabilities $\{\mathcal{K}\}$.

2. Optimisation process

The probability distribution associated with set \mathbf{e}_j by default is the weight of the set. We choose to use the strategy proposed in [43] to optimise the probability distribution $\{\mathcal{K}\}$ such that the variance of the estimator can be further minimised. We consider a diagonal approximation of $\text{Var}(\hat{\mathbf{o}})$, which is explicitly expressed as

$$l(\mathcal{K}) = \sum_l \frac{\alpha_l^2}{\chi(\mathbf{O}_l, \mathcal{K})}, \quad (50)$$

where $\chi(\mathbf{O}_l, \mathcal{K}) = \sum_{\mathbf{P}: \mathbf{O}_l \triangleright \mathbf{P}} \mathcal{K}(\mathbf{P})$ and $\mathcal{K} := (\mathcal{K}_1, \dots, \mathcal{K}_s)$ represents all the corresponding probabilities. In our experiment, since changing to another measurement basis requires a certain initialization time, we attempt to reduce the total number of basis sets to as few as possible. We delete observable sets with small weights. As such, we consider the final cost function as

$$l(\mathcal{K}) = \sum_{\mathbf{O}_l \in \mathcal{S}} \frac{\alpha_l^2}{\chi(\mathbf{O}_l)} + \sum_{\mathbf{O}_l \notin \mathcal{S}} \alpha_l^2 N_s, \quad (51)$$

where N_s is the total number of samples, $\mathbf{O}_l \in \mathcal{S}$ if there exists a set \mathbf{e} such that $\mathbf{O}_l \in \mathbf{e}$, and $\sum_{\mathbf{O}_l \notin \mathcal{S}}$ is the penalty caused by deleting some sets. The selection of the final cost function in Eq. (51) is inspired by the linear dependence of the variance and the number of samplings, which is indicated by Chebyshev inequality $N_s \geq \text{Var}(\hat{\mathbf{o}}) / (\delta \varepsilon^2)$. The regularised term $\alpha_j^2 N_s$ compensates the initial error ε_0 for excluding the observable \mathbf{O}_l in the estimation of \mathbf{O} . The initial error, which can be expressed as $\varepsilon_0 = |\sum_{j: \mathbf{O}_l \notin \mathcal{S}} \alpha_j \text{Tr}(\rho \mathbf{O}_j)|$, implies a bias of our estimation since \mathbf{O}_l will not be covered by any set.

It's important to note that we optimise the overlapped grouping strategy which was possibly used for comparison in [33] whose results appear pessimistic regarding the measurement cost. Specifically, we prioritise the measurement bases with large coefficients while discarding those with very small coefficients. This initial selection may introduce some level of error into our computations, termed initial errors. However, we can set a tolerance threshold and ensure the errors due to insufficient measurement bases are below such a threshold. This approach, while introducing certain errors, can significantly reduce the total number of measurements, and thus make it possible to run the algorithm on our device.

In our experiment, we reduce the total number of basis sets by decreasing the default number of samples N_s and cut down sets with a weight smaller than a threshold. This strategy will generate a small number of sets and could reduce

the running time for measurement. We could search for an optimised N_s in a real experiment with a small-scale input size with an initial N_{s0} . Since the cost function in Eq. (51) is not convex, we could find a local minimum solution using the nonconvex optimisation methods.

Since our overlapped grouping measurement strategy assumes measurements drawn from the probability distribution, the measurement accuracy may fluctuate. In our experiment, we derandomise the scheme by fixing the measurement basis \mathbf{P} . Suppose that we have determined the measurement basis sets $\mathcal{S} = \{e_1, \dots, e_s\}$ and the optimised probability distribution $\{(\mathbf{P}, \mathcal{K}(\mathbf{P}))\}$ using the above strategy. For the j th measurement \mathbf{P}_j with sampling probability \mathcal{K}_j , we choose the number of measurements for \mathbf{P}_j to be $\lfloor N_s \mathcal{K}_j \rfloor$, and select an additional one \mathbf{P}_j with probability $N_s \mathcal{K}_j - \lfloor N_s \mathcal{K}_j \rfloor$, where the total number of measurements is N_s .

With these improvement, in our experiment, the average number of shots for measuring the energy of H_2 , LiH , and F_2 is 1.3e5, 3.7e5, and 8.7e5, respectively, and the average running time for H_2 , LiH , and F_2 is 0.4min, 1.2min, and 2.9min, respectively.

III. ERROR-MITIGATED OBSERVABLE ESTIMATION

The VQE process requires the evaluation of gradient and energy. However, due to gate and measurement errors, these values unavoidably deviate from the ideal ones. It is crucial to mitigate the errors in order to get reliable results. In this section, we show how to obtain error-mitigated expectation values for observables.

A. Readout error mitigation

In experiments, we extract quantum state information by performing projective measurements on a computational basis and analysing the measurement outcomes. The quantum state $|\Psi\rangle$ collapses onto the computational basis $|i\rangle \in \{|0\rangle, |1\rangle\}^{\otimes N}$ with probability $p_i = |\langle i|\Psi\rangle|^2$ by Born's rule, which can be obtained by sampling the classical measurement outcomes. Getting unbiased probability $\{p_i\}$ is central for us to estimate the property of the quantum state. However, due to readout noise, the probability distribution deviates from the ideal one, which results in an error in the estimation. In what follows, we show how to mitigate the measurement readout errors.

The measurement error can be described as a classical random process, where any given ideal probabilistic measured result is transformed into a noisy one. Thus, the error can be fully described by a size $2^n \times 2^n$ transition matrix, also known as the calibration matrix Λ . The noisy measurement outcomes $\tilde{\mathbf{b}}_{\text{noisy}} = \{\tilde{b}_1, \dots, \tilde{b}_n\}$ is related to the ideal measurement outcomes $\mathbf{b}_{\text{ideal}} = \{b_1, \dots, b_n\}$ via the calibration matrix by

$$\tilde{\mathbf{b}}_{\text{noisy}} = \Lambda \mathbf{b}_{\text{ideal}}. \quad (52)$$

To circumvent the intractability of acquiring the complete calibration matrix, one can model the measurement error by taking tensor products of each local single-qubit calibration matrix of size 2×2 . The underlying assumption is that the measurement crosstalk in the quantum device is small enough that it can be completely omitted.

In our experiment, we optimise qubit-qubit residual coupling and readout parameters and check the correlated readout errors by random state measurement experiments. As shown in Fig. 8, correlated readout errors are negligible. Therefore, it is reasonable to assume that the measurement calibration matrix Λ admits a tensor product form as

$$\Lambda = \bigotimes_{j=1}^N \Lambda_j, \quad (53)$$

where Λ_j is the calibration matrix for the j th qubit, and it is expressed by

$$\Lambda_j = \begin{pmatrix} p(0|0) & p(0|1) \\ p(1|0) & p(1|1) \end{pmatrix} =: \begin{pmatrix} 1 - \epsilon_j & \gamma_j \\ \epsilon_j & 1 - \gamma_j \end{pmatrix}, \quad (54)$$

where $p(x|y)$ represents the probability of the measured basis is $|x\rangle$ given the prepared state $|y\rangle$ under computational bases $\{|0\rangle, |1\rangle\}$. With Eq. (54), $2n$ parameters, $\{\epsilon_j, \gamma_j\}$ for $j \in [1, n]$, can be used to describe the measurement error.

Next, we conduct the calibration process to learn the tensor product model parameters. We first select a set of product states \mathcal{T} . For each state $x \in \mathcal{T}$, we prepare the state on the quantum device and collect the measured product state y at each time for N_c times. We denote $m(y, x)$ as the number of times for y is observed when we prepare the

state x . Then, as shown in Ref. [64] the estimated two parameters ϵ_j and γ_j for the j th qubit is given by

$$\begin{aligned}\epsilon_j &= \frac{\sum_{x,y} m(y,x) \langle 1|y_j\rangle \langle x_j|0\rangle}{\sum_{x,y} m(y,x) \langle x_j|0\rangle}, \\ \gamma_j &= \frac{\sum_{x,y} m(y,x) \langle 0|y_j\rangle \langle x_j|1\rangle}{\sum_{x,y} m(y,x) \langle x_j|1\rangle}.\end{aligned}\quad (55)$$

Remark that to effectively learn the parameters, we are supposed to let the selected, prepared product state set \mathcal{T} contain at least once $x_j = 0$ and 1 for each qubit j .

The REM process essentially applies the inverse of Eq. (53) to the noisy measurement result for estimating the expectation value of an observable. Given an arbitrary Hermitian observable in the form of Eq. (43), and each \mathbf{O}_l can be expressed in a tensor product form, $\mathbf{O}_l = \bigotimes_{k=1}^N \mathbf{O}_l^k$, where \mathbf{O}_l^k acts on the k th qubit. The estimator of the expectation value of \mathbf{O}_l after REM is given by

$$\hat{\mathbf{o}}_l = \frac{1}{M} \sum_{m=1}^M \prod_{k=1}^N \langle e | \mathbf{O}_l^k \Lambda_k^{-1} | s_k^m \rangle, \quad (56)$$

where M is the measurement shots assigned for observable \mathbf{O}_l , $|e\rangle = |0\rangle + |1\rangle$, and $s_k^m \in \{0,1\}$ is the obtained measurement outcome for the k th qubit in the m th measurement.

Now, we discuss the estimator of the observable within the grouping measurement framework. Suppose we have determined the measurement basis set $\{\mathbf{P}_j\}$ and the associated measurement times N_j . Similarly to the grouping method, we denote \mathcal{S}_j containing all \mathbf{O}_l hit by \mathbf{P}_j (element-wise commute with \mathbf{P}_j). The estimator of the expectation value of the observable \mathbf{O} can be expressed by

$$\hat{\mathbf{o}} = \sum_l \alpha_l \hat{\mathbf{o}}_l, \quad (57)$$

where $\hat{\mathbf{o}}_l$ denotes the estimator of \mathbf{O}_l measured in basis \mathbf{P}_j . In our experiment, we estimate the expectation value of the observable \mathbf{O}_l by

$$\hat{\mathbf{o}}_l = \frac{\sum_{j:\mathbf{O}_l \triangleright \mathcal{S}_j} \hat{\mathbf{o}}_{l,j}}{s_l}. \quad (58)$$

Here, the denominator $s_l = \sum_j \delta_{\mathbf{O}_l \triangleright \mathcal{S}_j}$ is the total number of times \mathbf{O}_l being hit by \mathbf{P}_j . As such, the variance of $\hat{\mathbf{o}}$ with a single measurement can be estimated as

$$\text{Var}[\hat{\mathbf{o}}] = \sum_l \alpha_l^2 \frac{\sum_{j:\mathbf{O}_l \triangleright \mathcal{S}_j} \text{Var}[\hat{\mathbf{o}}_{l,j}]}{s_l^2}. \quad (59)$$

Without REM, when the observable \mathbf{O}_l is measured by \mathbf{P}_j , it yields two potential outcomes: either $+1$ or -1 . Let $t_{l,j}$ represent the count of measurements resulting in an outcome of $+1$. It is straightforward to see that the measurement result (i.e. estimator) associated with the measurement \mathbf{P}_j for observable \mathbf{O}_l is $\hat{\mathbf{o}}_{l,j} = 2t_{l,j}/N_j - 1$.

With REM, $\hat{\mathbf{o}}_{l,j}$ is given by Eq. (56). For later convenience, we give the explicit form of the observable estimation as

$$\hat{\mathbf{o}}_l^{\text{REM}} = \frac{1}{N_j} \sum_{j:\mathbf{O}_l \triangleright \mathcal{S}_j} \sum_{m=1}^{N_j} \prod_{k=1}^N \langle e | \mathbf{O}_l^k \Lambda_k^{-1} | s_k^m \rangle. \quad (60)$$

It is thus straightforward that the readout error mitigated estimator of the expectation value of observable \mathbf{O} can be explicitly expressed as

$$\hat{\mathbf{o}}^{\text{REM}} = \sum_l \frac{\alpha_l}{s_l} \sum_{j:\mathbf{O}_l \triangleright \mathcal{S}_j} \sum_{m=1}^{N_j} \prod_{k=1}^N \langle e | \mathbf{O}_l^k \Lambda_k^{-1} | s_k^m \rangle. \quad (61)$$

The readout error mitigated estimation in Eq. (61) is unbiased if every observable is assigned at least one measurement basis $N_j \geq 1$, otherwise, the estimation has an initial error.

B. Gate error learning by Clifford fitting

1. Methods

We consider Clifford fitting (also called Clifford data regression) [65] to mitigate the dominant CZ gate error. The key idea is to obtain an error-mitigated expectation value by fitting a regression function f^{CF} which maps a noisy expectation value to an error-mitigated one as

$$o^{\text{ideal}} = f^{\text{CF}}(o^{\text{noisy}}).$$

The regression function is obtained in a learning style using data pairs of ideal and noisy results generated from classically simulable (near)-Clifford circuits and noisy quantum circuits. Here, we choose the fitting function to be linear,

$$f^{\text{CF}}(\cdot) = a(\cdot) + b,$$

where a and b are the coefficients to be fitted.

For Clifford fitting in quantum chemistry simulation, which relies on a parameterised quantum circuit, we choose a collection of quantum circuits by randomly replacing the parameterised gates with Clifford gates, and the remaining parameterised gates are assigned with a rotating angle choosing independently, uniformly from $[0, 2\pi]$. Here, we denote n_p as the total number of parameterised gates in a parameterised quantum circuit, K as the number of gates not being substituted, and $S_u = \{u_i\}$ as the set of the randomly assigned circuit. Hence, the remaining $n_p - K$ gates are replaced with single-qubit Clifford gates.

For a given Pauli observable $\mathbf{O}_j \in P^{\otimes n} \setminus I^{\otimes n}$ with $P \in \{I, X, Y, Z\}$, we aim to establish a training data set consists of data pairs of ideal expectation value simulated on a classical computer and noisy value measured from the quantum device with the set of quantum circuits we construct above. For efficient classical simulation, it is crucial that they are “nearly Clifford” in the sense that the stabiliser rank, i.e. the number of non-Clifford gates K in the quantum circuit, of each quantum circuit is a constant. In this case, these quantum circuits can be simulated classically [66]. Compared to other error mitigation methods, such as zero noise extrapolation approaches, the Clifford fitting method does not require stretching the implementation time of the gates. Besides, the effect of noise on the training and corresponding testing (experimental) circuit on the expectation values of observables is expected to remain the same as only single-qubit rotation gates are replaced by Clifford gates through changing the rotation angle and the two-qubit CZ gates are unchanged.

2. Experimental procedure

For our goal to estimate the energy, we run the Clifford fitting process for each observable in the Hamiltonian. The number of quantum circuits could be enormous and impractical for experimental realisation. Here, we discuss how to reduce instances of the circuit to be implemented for Clifford fitting.

We observe that in practical computation, some observables’ expectation values remain unchanged or change in a negligible small range for different parameters in different quantum circuits, called unchanged observables. It is, therefore, unnecessary to run the algorithm for these unchanged observables on quantum hardware, upon evaluating the energy of the quantum system. We elaborate on the complete protocol in the following.

1. In the first step, we identify and record all the changed and unchanged observables in the Hamiltonian. For each Pauli observable \mathbf{O}_j in the Hamiltonian \hat{H} , randomly assign all the parameters uniformly from $[0, 2\pi]$ and obtain a L -size quantum circuit instance set $\mathcal{S}_u^{(Z)} = \{u_i\}_{i=1}^L$, where the upper-script Z stands for the number of non-Clifford gates in the circuit, and u_i denotes the i th quantum circuit instance obtained from the random-parameter assignment. The size L needs to be sufficiently large to create enough quantum circuit instances to determine if the expected value of an observable changes. Compute the expectation value $\{\langle \mathbf{O}_j \rangle_{u_i}\}_{i=1}^L$ classically for each circuit instance in $\mathcal{S}_u^{(Z)}$ for each observable. Compute the range value σ_j and the variance μ_j of the expectation values. If both σ_j and μ_j are greater than the thresholds σ_T and μ_T we chose, then \mathbf{O}_j is labelled as a changed observable, otherwise, an unchanged observable. We record the invariant observables, which will not be measured on quantum hardware. Record its value for estimating the energy in the final step.
2. Let M be the total number of parameterised gates. Randomly choose K out of M parameterised gates and assign value independently to each parameter from $[0, 2\pi]$ to construct the quantum circuits set $\mathcal{S}_u^{(K)}$ of size R . Set the left $M - K$ gates to the identity gate. R is chosen to be sufficient for fitting a line for the linear regression, such as 10.

3. We refer to the set of changed observables as $\{O_C\}$, run step 4 for each observable in O_C . Then go to step 5.
4. For a given observable \mathbf{O}_j , calculate the ideal expected value $\{\langle \mathbf{O}_j \rangle_{u_i}\}_{i=1}^R$ with respect to state prepared by each u_i . Here, we want the ideal values to be as spread out between $[-1, 1]$ as possible. The purpose is that at least these different instances will appear in different intervals so that the values are dispersed enough for better linear regression. To this end, we classify different expected values according to their intervals, such as selecting instances in the intervals of $[-1, 0.9]$, $[-0.9, 0.8]$, \dots , $[0.9, 1]$.
5. Set $\{O_S\} = \emptyset$. Update $\{O_S\}$ by adding all the observables that satisfy the dispersion condition in step 4. Repeat step 4 for multiple times for observables in $\{O_C\} \cap \overline{\{O_S\}}$ until $\{O_C\} \cap \overline{\{O_S\}}$ is empty. At each repetition, add qualified observables to $\{O_S\}$, and record the quantum circuit set $\mathcal{S}_u^{(K)}$ as well.
6. For each recorded quantum circuit run on the quantum device to get the noisy expectation value for all its corresponding observables. For each observable O , feed the ideal and corresponding noisy value to fit the linear regression function and optimise the loss function

$$C = \sum_{\phi_i \in \mathcal{S}_\psi^{(K)}} \left(\langle O \rangle_{u_i}^{\text{exact}} - \left(a \langle O \rangle_{u_i}^{\text{noisy}} + b \right) \right)^2. \quad (62)$$

Therefore we get different linear mapping functions for different observables.

7. Use the fitting function to mitigate the error in expectation value for the corresponding observable.

The estimation of an observable \mathbf{O} can be obtained by Eq. (57), and is formally expressed as

$$\hat{\mathbf{o}}^{\text{CF}} = \sum_l \alpha_l \hat{\mathbf{o}}_l^{\text{CF}}, \quad (63)$$

where the estimator for \mathbf{O}_l after REM and CF is given by

$$\hat{\mathbf{o}}_l^{\text{CF}} = f_l^{\text{CF}}(\hat{\mathbf{o}}_l^{\text{REM}}), \quad (64)$$

and f_l is the fitting function associated with \mathbf{O}_l .

C. Symmetry verification

Error mitigation by symmetry verification takes advantage of prior knowledge of the physical subspace where we search for the solution to the problem. There are two types of symmetries in the molecular problems considered here, which are the conservation of particle number and singlet state for the ground state, need to be satisfied. The particle number, hence the parity, of the ground state should be conserved throughout the simulation process. In addition, it is known in the quantum chemistry community that for closed-shell molecules, the ground state is bound to be a spin singlet state.

Below, we briefly review error mitigation by symmetry verification introduced in [46]. For each symmetry verification operator \hat{S}_i , we have,

$$\hat{S}_i |\psi\rangle = s_i |\psi\rangle, \quad (65)$$

where the $s_i \in \pm 1$. The density matrix, which is projected into the subspace that conserves the symmetry, can be expressed as,

$$\rho_{s_i} = \frac{\Pi_{s_i} \rho \Pi_{s_i}}{\text{Tr}(\Pi_{s_i} \rho)}, \quad (66)$$

with $\Pi_{s_i} = \frac{I + s_i \hat{S}_i}{2}$. Specifically, as a result of the closed shell molecule that we deal with, the trial wave function we pick is in an even-parity sub-manifold for total particle number and spin. Therefore, the eigenvalues of parity check operators for the correct symmetry are always one, i.e., $s_i = 1$. We project the target molecular Hamiltonian H to the even-parity subspace. For this purpose, we have

$$\text{Tr}(\hat{H} \rho_{s_i}) = \frac{\text{Tr}(\hat{H} \rho) + \text{Tr}(\hat{H} \hat{S}_i \rho)}{1 + \text{Tr}(\hat{S}_i \rho)}, \quad (67)$$

which effectively conserves the symmetry of the quantum subspace. This is achieved by measuring $\text{Tr}(H\rho)$, $\text{Tr}(H\hat{S}_i\rho)$, and $\text{Tr}(\hat{S}_i\rho)$.

We have the particle number or parity conservation for the molecular problems considered here, i.e., $[\hat{H}, \hat{S}] = 0$ with $\hat{S} = \bigotimes_i \hat{Z}_i$. This symmetry verification expands the to-be-measured observable set, which is composed of the elements in the decomposition of H and $H\hat{S}$. The symmetry verification EM has three ingredients $\langle \hat{H} \rangle$, $\langle \hat{H}\hat{S} \rangle$, and $\langle \hat{S} \rangle$. Each of them is estimated by measuring the predetermined basis, introduced in Sec. II E. The final error mitigated results by SV are computed classically by Eq. (67) as

$$\hat{\mathbf{o}} = \frac{\langle \hat{H} \rangle^{\text{CF}} + \langle \hat{H}\hat{S} \rangle^{\text{CF}}}{1 + \langle \hat{S} \rangle^{\text{CF}}}. \quad (68)$$

Here, $\langle \hat{H} \rangle^{\text{CF}}$, $\langle \hat{H}\hat{S} \rangle^{\text{CF}}$, and $\langle \hat{S} \rangle^{\text{CF}}$ are the estimator obtained by sequentially applying REM in Eq. (60) and CF in Eq. (63), and classical post-processing by Eq. (57).

In our experiment, we found that a combination of Clifford fitting and symmetry verification might not perform well. This is because, in our experiment, symmetry verification requires measuring many large-support observables, which demands high-precision measurement for these observables. In Fig. 18, we study the performance of symmetry verification and explain why it results in large fluctuations in the energy estimation, which will be elaborated on below.

D. Connected moments expansion

The connected moments expansion (CMX) method [67] is derived from the imaginary time evolution (ITE) approach that can be expressed in the following formula

$$E(\beta) = \frac{\langle \Phi | H e^{-\beta \hat{H}} | \Phi \rangle}{\langle \Phi | e^{-\beta \hat{H}} | \Phi \rangle} = \sum_{k=0}^{\infty} \frac{(-\beta)^k I_{k+1}}{k!}, \quad (69)$$

where β is the evolution time of the ITE method, and we expand the formula as the expansion of the connected moments I_k taking advantage of the Taylor expansion. The mechanism of the ITE method is to project the state $|\Psi\rangle$ towards the ground state of H , and Eq. (69) gives the exact ground state energy as β goes to infinity as long as the state $|\Psi\rangle$ is non-orthogonal to the ground state. The evolution time β in practice is chosen to be a finite number and is essentially related to the overlap between the state $|\Psi\rangle$ and the ground state.

The ITE operator $e^{-\beta \hat{H}}$ is nonunitary and thus generally hard to implement on a quantum device. The CMX method provides a way to circumvent this problem through measuring the higher moments of \hat{H} in Eq. (69). Specifically, the connected moment is defined recursively by

$$I_k = \langle \Phi | \hat{H}^k | \Phi \rangle - \sum_{i=0}^{k-2} \binom{k-1}{i} I_{i+1} \langle \Phi | \hat{H}^{k-i-1} | \Phi \rangle. \quad (70)$$

The analytical form for exact energy as β goes to infinity can be represented by

$$E_{\text{ground}} = I_1 - \frac{S_{2,1}^2}{S_{3,1}} \left(1 + \frac{S_{2,2}^2}{S_{2,1}^2 S_{3,2}} \dots \left(1 + \frac{S_{2,m}^2}{S_{2,m-1}^2 S_{3,m}} \right) \dots \right), \quad (71)$$

where $S_{k,1} = I_k$, $S_{k,i+1} = S_{k,1} S_{k+2,i} - S_{k+1,i}^2$ and it is straightforward to have $S_{2,1} = I_2 = \langle \hat{H}^2 \rangle - \langle \hat{H} \rangle^2$ and $S_{3,1} = \langle \hat{H}^3 \rangle - 3 \langle \hat{H} \rangle \langle \hat{H}^2 \rangle + 2 \langle \hat{H} \rangle^3$. For practical concerns, one truncates the expansion up some order k . In our experiment, we measure the higher-order moment $\langle \Phi | H^k | \Phi \rangle$ for $k \leq 3$ using the grouping measurement schemes introduced in Sec. II E. It is reasonable for our choice of $k \leq 3$ in that we expect the application of various quantum error mitigation (QEM) methods to be able to reproduce most parts of the ground state energy, but in some cases, it may not be able to reach the chemical-accuracy requirement. As such, the state we prepared in the energy estimation step corresponds to an effective state which has a fairly good overlap with the ground state, but is not exactly the same. Assuming to perform the ITE approach in this case, it follows that the evolution time β of the ITE method can be chosen to a relatively small one. Thus one can equivalently truncate the expansion Eq. (70) up to some constant order as the expansion is monotonically decreasing. Truncating the expansion to a low order also makes the method

affordable experimentally. Note that CMX is not a variational method, and thus the energies obtained by CMX may be lower than the true ground state energy.

In the experiment, after the VQE procedure, we would obtain the final circuit parameters. We then execute the circuit under different measurement bases to measure the expectation values of different observables (\hat{H} , \hat{H}^2 and \hat{H}^3). Finally, the ground state energy is estimated by Eq. (71).

The variance of the energy estimation using the connected moments' expansion up to the second order is calculated by

$$\text{Var}[E_{\text{ground}}] = \left(\frac{\partial E_{\text{ground}}}{\partial a}\right)^2 \text{Var}[a] + \left(\frac{\partial E_{\text{ground}}}{\partial b}\right)^2 \text{Var}[b] + \left(\frac{\partial E_{\text{ground}}}{\partial c}\right)^2 \text{Var}[c], \quad (72)$$

and it takes the form of

$$\text{Var}[E_{\text{ground}}] = \left(1 + \frac{4aS_{2,1}}{S_{3,1}} - \frac{S_{2,1}^2(-3b + 6a^2)}{S_{3,1}^2}\right)^2 \text{Var}[a] + \left(\frac{2S_{2,1}}{S_{3,1}} + \frac{3S_{2,1}^2 a}{S_{3,1}^2}\right)^2 \text{Var}[b] + \frac{S_{2,1}^4}{S_{3,1}^4} \text{Var}[c] \quad (73)$$

where we have defined $a := \langle \hat{H} \rangle$, $b := \langle \hat{H}^2 \rangle$ and $c := \langle \hat{H}^3 \rangle$. It is worth noting that this calculation for the variance is based on the variance propagation, and the actual variance could be smaller. The error bar for the energy estimation using CMX is calculated according to Eq. (73).

E. Experimental procedure for observable estimation

In the experiment, according to the target observable set, $\{\mathbf{O}_l\}$, including the Hamiltonian \hat{H} , the symmetry verified Hamiltonian $\hat{H}\hat{S}$, parity \hat{S} , and the Hamiltonian power \hat{H}^k , the measurement basis $\{\mathbf{P}\}$ and the associated measurement shots are generated using the method introduced in Sec. II E. The experimental procedure for obtaining error-mitigated observable estimation in order is summarised as follows.

1. Experimental benchmark for measurement noise. Test whether the measurement errors admit a tensor product type by random state measurement. Obtain the calibration matrix Λ by measurement error calibration.
2. Generate a series of random quantum circuits for Clifford noise learning. Measure the state prepared by Clifford circuits in the predetermined basis $\{\mathbf{P}\}$ and obtain the fitting function f^{CF} for each observable.
3. During the VQE process, measure the observable on the state in basis $\{\mathbf{P}\}$. For each \mathbf{O}_l , apply readout error mitigation by Eq. (60). Get the observable estimation after CF in Eq. (63) or Eq. (64).
4. Get symmetry verified results using Eq. (67). In our experiment, we apply symmetry verification to correct the energy for H_2 and LiH .
5. The final ground state energy is estimated using the CMX in Eq. (71).

IV. EXPERIMENTAL IMPLEMENTATION AND RESULTS

In Sec. , we show how to optimise the Zuchongzhi processor to obtain high-fidelity gates and readout. In Sec. II, we discuss quantum algorithms for the ground state search and quantum state measurement with fewer quantum resources. Subsequently, in Sec. III, we show how to obtain error-mitigated ground state energy estimation. With these experimental and theoretical advances, we study systematically the ground state energy estimation for three molecules, H_2 , LiH , F_2 . Finally, we point out the challenges in experimental quantum computational chemistry.

A. Experimental procedure

Benchmarking:

Prior to experiments, we first calibrate the qubits and couplers set used in our experiment to obtain the performance with high enough gate fidelity and readout fidelity, as well as to ensure there are no correlated readout errors. The calibrations contain the following steps.

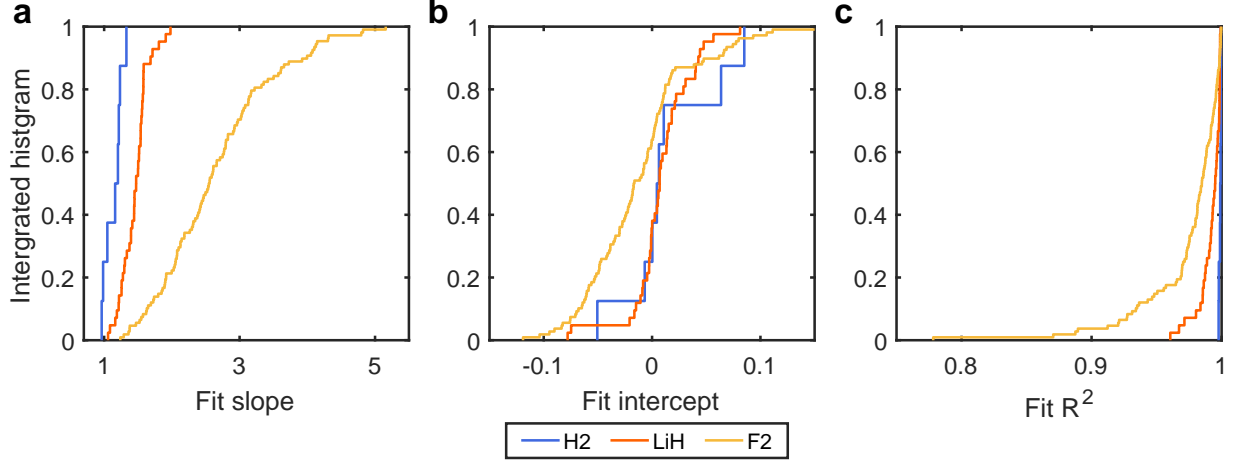


FIG. 15. **Distribution of Clifford fit parameters.** The accumulated distribution of slope, intercept and goodness of fit for H₂ (R=2.6), LiH (R=1.5) and F₂ (R=2.0) are shown in the diagram. With the system size and circuit depth increasing, we can observe that (a) the slopes of Clifford fit become larger due to the impact of decoherence. (b) the variance of intercept becomes larger, and the mean value is off zero, which may be caused by gate correlated errors. (c) the goodness of fit becomes worse. Two main issues may cause it. One is gate-correlated errors that make our model nonlinear. The other is insufficient fit data, which will increase our experiment resources.

1. Calibrate the qubit frequency and Rabi amplitude, update the readout IQ clouds discrimination lines and the readout error mitigation (REM) matrix by standard readout experiment. The REM matrix for single-qubit is described as Eq. (54), where $p(x|y)$ represents the probability of the measured basis is $|x\rangle$ given the prepared state $|y\rangle$ under computational bases $\{|0\rangle, |1\rangle\}$. We prepare the qubit in $|0\rangle$ and $|1\rangle$ in the experiment and select the perpendicular bisector of the two IQ clouds centres as the discrimination line to separate the $|0\rangle$ and $|1\rangle$ as well as acquire $p(x|y)$. This step runs prior to each VQE experiment for a molecule with a single bond length, as well as before every complete experiment for calibration and benchmark.
2. Benchmark single-qubit and CZ gates, and update the control parameters in CZ gates. Count the fidelities for all single-qubit gates and CZ gates, and ensure the fidelities are high enough and stable. This step will be run every 3 hours.
3. Check the correlated readout error. Comparing the average union readout fidelity and standard readout fidelity with the random state readout experiment to check whether the corrected readout error is negligible. This step will also be run every 3 hours.

Experiments:

A crucial step in optimisation is to get the gradient with respect to a parameter, which is estimated by measuring the parameter-shifted quantum state, as indicated by Eq. (40). We apply error mitigation techniques, including REM, CF, and SV, to obtain an error-mitigated gradient and energy. In the following, we elaborate on the experimental procedures. The experimental Clifford fitting is composed of the following steps:

1. Determine a set of Clifford circuits with the random parameters generated using the method described in Sec. III B. For each Pauli measurement basis \mathbf{P}_j and the associated observable set $\mathbf{e}_j = \{\mathbf{O}_l | \mathbf{O}_l \triangleright \mathbf{P}_j\}$, record instances of quantum circuit \mathcal{C}_j . Note that \mathcal{C}_j could be identical to make the experiments friendly.
2. Run noisy Clifford circuits $\{\mathcal{C}_j\}$ with the pre-determined random parameters. Measure in Pauli basis $\{\mathbf{P}\}$ generated using the overlapped grouping methods in Sec. II E and record the noisy expectation value for each observable \mathbf{O}_l .
3. Simulate Clifford circuits $\{\mathcal{C}_j\}$ classically and record the ideal expectation value for every observable.
4. Fitting the ideal and noisy expectation value with a linear function $f_l^{\text{CF}}(\cdot) = a(\cdot) + b$ for every observable, we get the error mitigation function. Record those fitting functions f_l^{CF} , and we could use them to mitigate the errors in the observable estimation by Eq. (64).

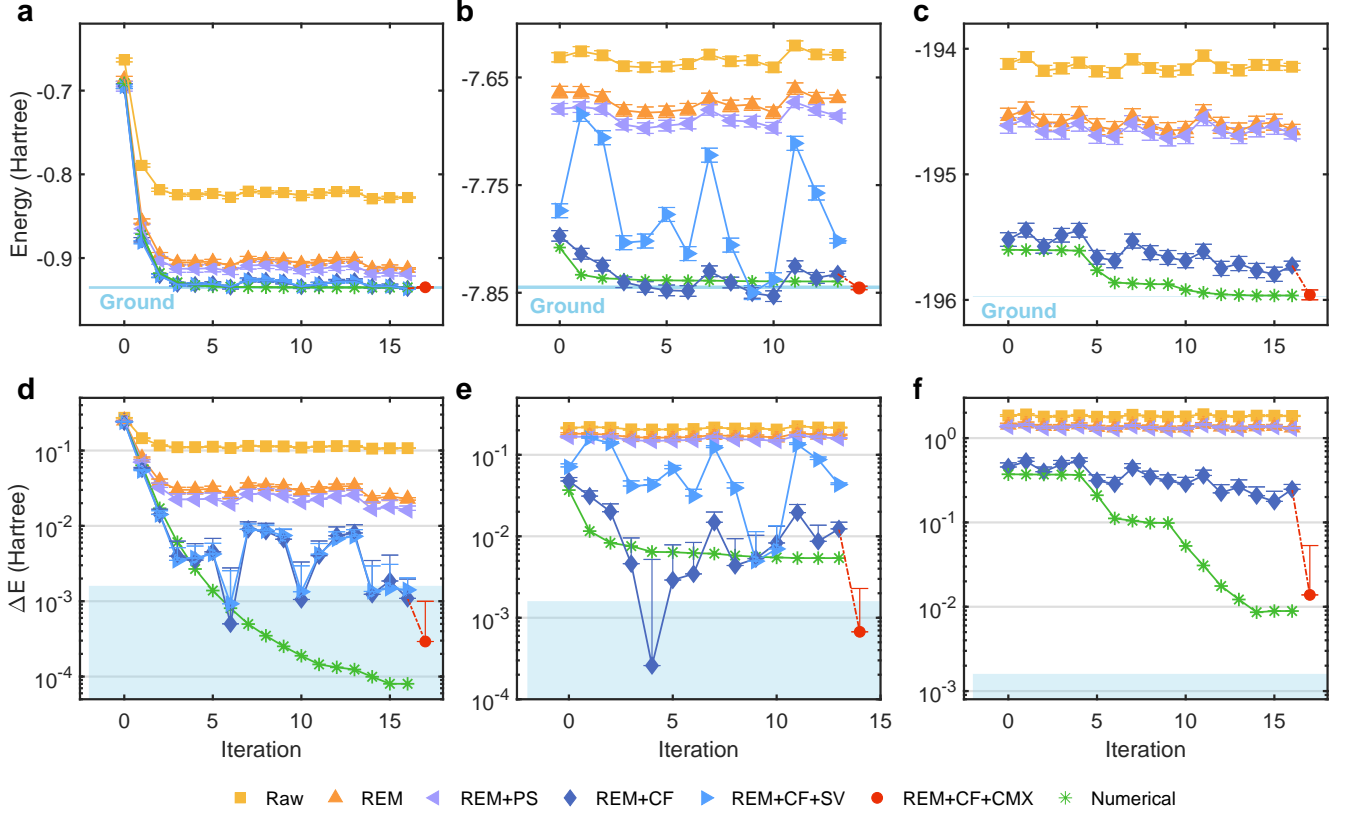


FIG. 16. **Optimisation procedure.** The optimisation procedure traces of energy and abs energy error for H_2 ($R=2.6$), LiH ($R=2.2$) and F_2 ($R=2.6$) are shown in the picture. Here in (a)(b)(c), we add energy with REM + PS (purple leftward triangles), while the others are the same as in Figure 2b. Figure (d)(e)(f) show the traces of abs energy error during the optimisation procedure.

In the VQE experiment, we first prepare the initial state as a Hartree-Fock state or multi-reference state which is described in Sec. II B. Then, we measure the Hamiltonian to get the initial state energy E_0^{expm} . In our experiment, the observables are measured in Pauli bases, which are generated using the overlapped grouping strategy introduced in Sec. II E. We search the ground state by optimising the parameters in the circuit. A key component in our VQE experiment is to get the error-mitigated expectation value for observables. To do so, we apply the above error mitigation schemes for each measurement outcome. The experimental procedures for error mitigation have been shown in Sec. III E

The VQE optimisation is summarised as follows:

1. Gradient estimation and optimisation. Determine θ associated with the single-qubit Pauli-rotation gate, in which we select $N/2$ parameters to update. For each selected parameter, the gradient is estimated using Eq. (40), which requires measuring the Hamiltonian on the parameter-shifted state. Get the gradient for all selected parameters and update the parameters. Here, we obtain the error-mitigated measurement outcome $\mathcal{L}(\theta^\pm)$ defined in Eq. II D by REM and CF error mitigation schemes.
2. For each iteration, we measure the energy with the updated parameters and hence record the optimisation trace.
3. Run the 1 and 2 steps to update the parameters until convergence. For all the molecules, the energy converges within 15 iterations.

Finally, we measure the state with the optimised parameters. We correct the ground state energy using connected moments expansion (CMX), which requires measuring $\langle \hat{H}^2 \rangle$ and $\langle \hat{H}^3 \rangle$, as described in Sec. III D. The expectation value of $\langle \hat{H}^k \rangle$ for $k \leq 3$ will be measured and then error mitigated in a similar fashion to that of $\langle \hat{H} \rangle$. With the error mitigated results, we calculate the CMX energy using equations Eq. (70) and Eq. (71).

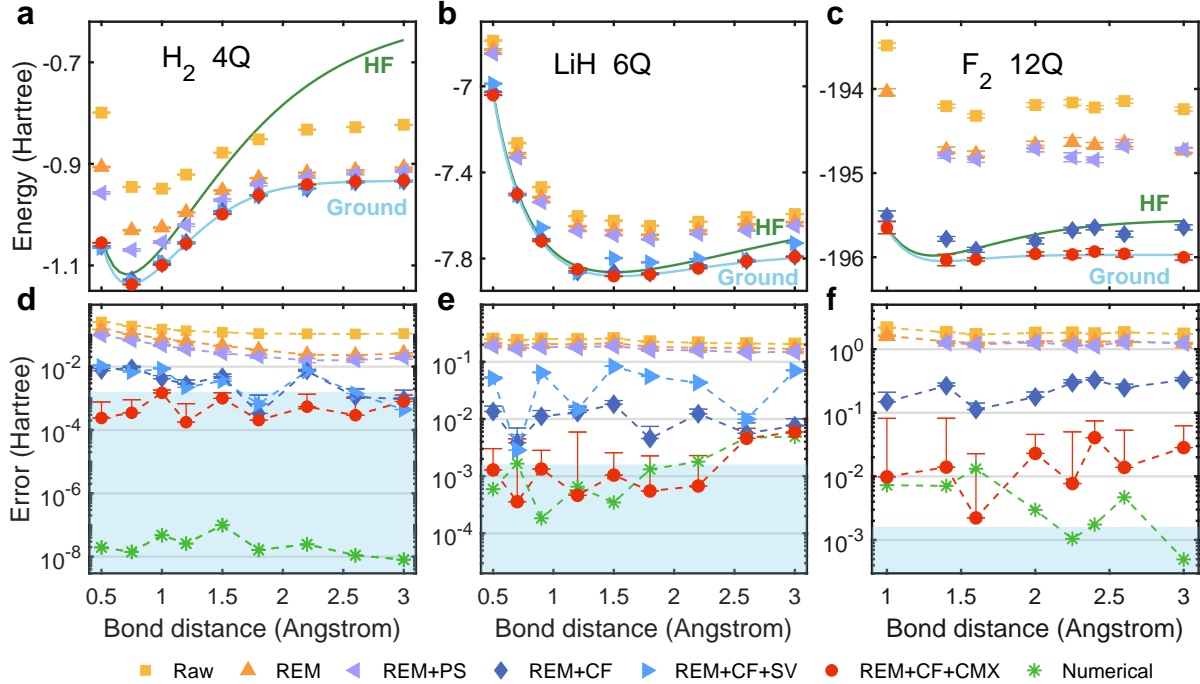


FIG. 17. **The VQE simulations for potential energy curves for different molecules.** Similar to Figure 3, more results with different error mitigation strategies are shown here. (a-c) Potential energy curves as functions of the bond distance for H_2 (4 qubits), LiH (6 qubits) and F_2 (12 qubits) molecules with various error mitigation strategies. (d-f) Absolute errors are compared to the FCI results. We compare the raw data (yellow squares) with the application of REM (orange triangles), REM and PS (purple triangles), REM and CF (deep blue diamonds), SV (blue triangles) and CMX (red circles). The results marked by green asterisks are energies calculated by classical simulation with the parameters searched in the experiment. The ground state energy with chemical accuracy (blue regime) is calculated theoretically as a reference.

B. Results

This section shows experimental results for the ground state search and ground state energy estimation.

We select at most 12 qubits on the Zuchongzhi 2.0 quantum processor. Several patterns of 12 qubits are available in our processor. Different pattern choices could lead to significantly different results in our experiment. Since learning the gate error is crucial in our experiment, we run the Clifford fitting experiment with different qubit patterns to characterise the performance and finally select the pattern based on the goodness of fit and the fit slope.

We first select three bond distances for different molecules, including H_2 ($R=2.6$), LiH ($R=2.2$) and F_2 ($R=2.6$), to study the performance of the Clifford fitting. Fig. 15 shows the performance of the Clifford fitting for the three molecules at the selected bond distances by the accumulated distribution of the slope, intercept, and the R^2 value. Through the comparison of a, b, and c, we find that the fitting becomes worse with the system size increases, which may be attributed to the correlated gate errors and the fluctuations of the data.

Then, we show the ground state searching with the variational algorithms for the three molecules. We show the optimisation processes for H_2 ($R=2.6$), LiH ($R=2.2$) and F_2 ($R=2.6$) in Fig. 16. The figure presents error-mitigated energy estimations with different error mitigation schemes, including REM, PS, CF, SV, CMX, and their combinations. Fig. 16 shows that although measured energies (yellow square) have fluctuations, energies after applying the combination of REM and CF clearly improve the energy accuracy along the optimisation. Error-mitigated energies tend to decrease consistently in successive iterations.

Next, we show the calculation of potential energy curves in Fig. 17. Fig. 17a, b, c show the energy iteration during the VQE optimisation process for H_2 ($R=2.6$), LiH ($R=1.5$) and F_2 ($R=2.0$), respectively. These results provide a much more detailed comparison of the error mitigation schemes used in the experiment. In the following, we discuss the performance of these error mitigation schemes.

We first discuss error mitigation with symmetry verification. As can be found in Fig. 16 and Fig. 17, SV results in a large fluctuation in the energy estimation. In particular, as illustrated in Fig. 17(b), the energy with REM, CF and

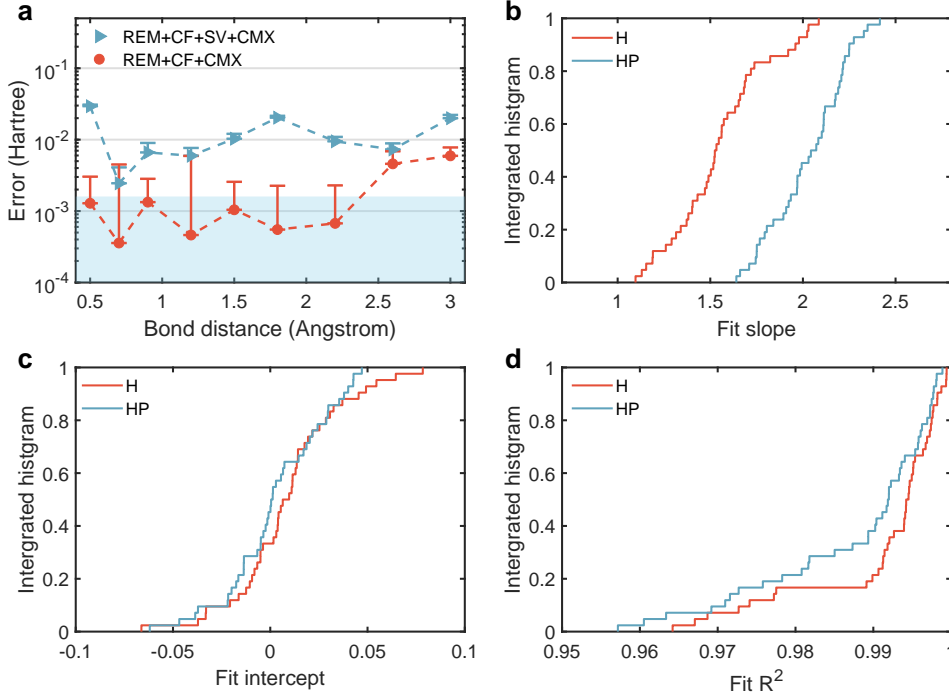


FIG. 18. **Symmetry Verification.** (a) The comparison of the abs energy error with different error mitigation setups for LiH. The red dot is the energy with REM + Clifford fitting + CMX, and the grey-blue triangle is the energy with REM + Clifford fitting + CMX + SV. (b)(c)(d) are the slope, intercept and R^2 of the LiH($R = 2.2$), respectively. “H” refers to the original Hamiltonian \hat{H} and “HP” refers to the symmetry verified Hamiltonian $\hat{H}\hat{S}$.

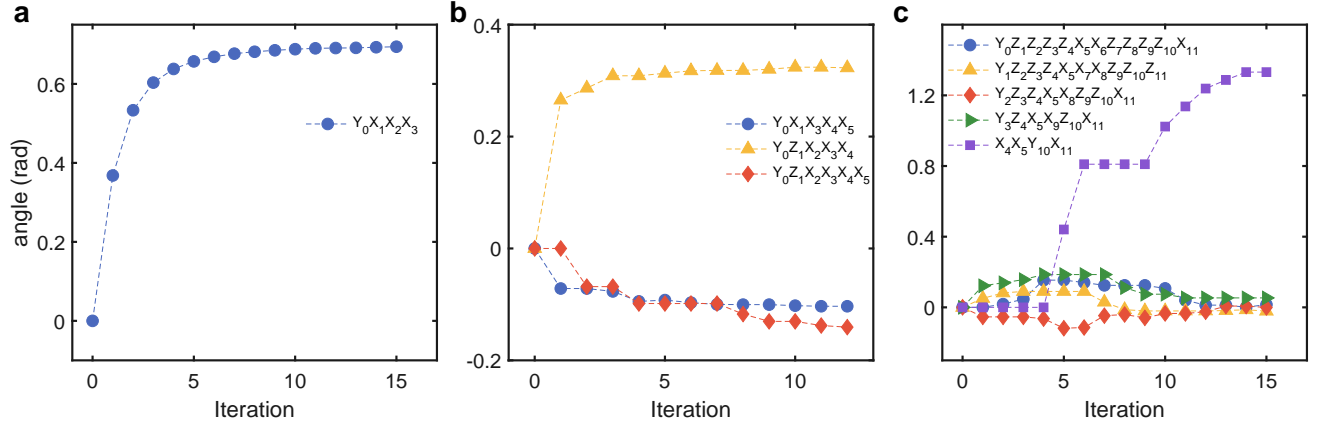


FIG. 19. **Parameter optimisation processes.** The evolution of variational parameters in optimisation processes for H_2 (a), LiH (b) and F_2 (c), respectively. For each iteration, we select $N/2$ parameters to update, and the parameter converges within 15 iterations for all the molecules.

SV (grey right triangles) have a greater fluctuation than REM + CF during the optimisation procedure. The energy with REM, CF and SV show a larger error than REM and CF for all bond distances, as can be found in Fig. 18(a). This can be understood as follows. The fitting coefficient for the symmetry verified Hamiltonian $\hat{H}\hat{S}$ is much larger than \hat{H} and thus results in large fluctuation after applying the combination of CF and SV. This is verified by the slope in Fig. 18b and the fitting performance in Fig. 18d.

These results indicate the combination of SV and CF could bring a large fluctuation. Therefore, we mainly focused on the readout error mitigation, Clifford fitting and ground state energy correction by using connected moment expansion in the main text, while we did not show the results energy of LiH and F_2 using symmetry verification.

In addition, we add the energy with REM and post-selection (PS). In this scheme, the measurement result of $Z^{\otimes n}$ Pauli basis is post-selected based on the conservation of particle numbers, and other Pauli bases are still error-mitigated with REM. The REM and post-selection (PS) energy perform better than single REM yet worse than REM and CF. With an increasing system size, a combination of REM and PS shows diminishing energy accuracy improvements, implying PS is not a suitable error mitigation strategy for scalable quantum computational chemistry.

Finally, we show the performance of VQE after the optimisation process. Fig. 20 shows the relative error compared to the initial energy for the three molecules at different bond distances. The relative error compared to the initial state energy is calculated by

$$\frac{E_i - E_{\text{ground}}}{E_0^{\text{expm}} - E_{\text{ground}}}, \quad (74)$$

where E_i is the error-mitigated energy or the energy, which is computed using the parameters that are found until convergence, E_0^{expm} is the energy measured on the initial state, E_{ground} is the ideal ground state energy. This relative error characterises the improvement with respect to the initial state energy by VQE.

We can see from Fig. 20 that compared to the initial state energy, the relative average energy errors with only REM for the three molecules are 28.98%, 78.86% and 75.42%.

The results are improved by 0.278%, 0.778% (0.326% except R2.6 and R3.0), and 1.00% for molecules with REM+CF+CMX EM schemes, and by 1.56×10^{-7} , 0.783% (0.392% except R2.6 and R3.0), and 0.268% for numerical result. The average absolute error associated with different methods, including REM, REM + PS, REM+CF+SV, REM+CF, REM+CF+CMX, and numerical, are displayed in Table I.

Molecules	Raw	REM	REM + PS	REM+CF+SV	REM+CF	REM+CF+CMX	Numerical
H ₂ (milli-Hartree)	143.661 ± 0.807	60.580 ± 1.015	38.650 ± 2.367	4.552 ± 0.740	4.254 ± 0.997	0.565 ± 0.542	2.96×10^{-5}
LiH (milli-Hartree)	233.564 ± 2.704	191.358 ± 3.313	169.987 ± 3.110	43.888 ± 2.383	9.965 ± 2.923	1.802 ± 2.423	1.794
F ₂ (Hartree)	1.8315 ± 0.0264	1.3419 ± 0.0387	1.2231 ± 0.0382	–	0.2378 ± 0.0354	0.0174 ± 0.0417	0.0048

TABLE I. Comparison of average absolute energy error for H₂, LiH and F₂ using different error mitigation schemes. The first two rows use milli-Hartree.

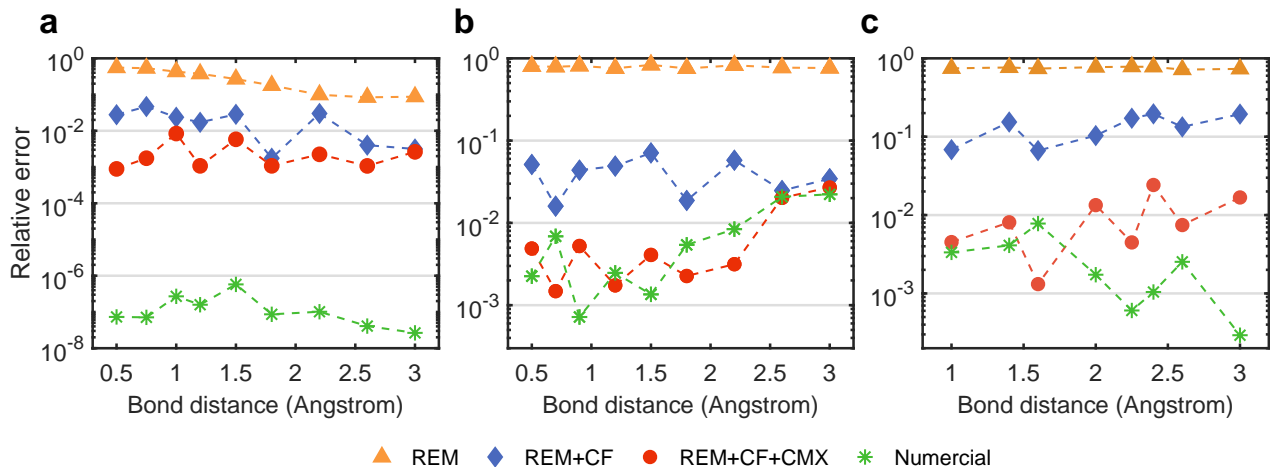


FIG. 20. **Relative error compared to the initial state energy.** Relative errors for H₂, LiH and F₂ with different error mitigation schemes, only REM (yellow triangles), REM and Clifford fitting schemes (blue diamonds), REM and Clifford fitting and CMX (red circles), the numerical result (green stars).

C. Parameters iteration

In Fig. 19, we present the parameters iteration for H₂ (R=2.6), LiH (R=1.5) and F₂ (R=2.0). For H₂, LiH and F₂, there are 1, 3 and 5 parameters in total to iterate respectively. All parameters are optimised from zero. 1, 2 and 3

parameters are randomly selected to optimise during each iteration for H₂, LiH and F₂, respectively. All optimisation runs for 5 to 15 iterations.

D. Noise analysis

In this section, we analyse the noise effect in our chemistry simulation. We assume noise in the circuit can be described by a depolarising channel

$$\mathcal{E}(\rho) = p\rho + (1 - p)\frac{I}{2^N}, \quad (75)$$

where $1 - p$ characterises the error rate, and p characterises the fidelity of the quantum state. Under depolarising noise, the energy is given by

$$E^{\text{noisy}} = \text{Tr}(\rho^{\text{ideal}}\hat{H}) = p\text{Tr}(\rho^{\text{ideal}}) = pE^{\text{ideal}}. \quad (76)$$

Here, the identity operator in the Hamiltonian has been excluded so that $\text{Tr}(\hat{H}) = 0$. We can get the error rate p by fitting the measured energies E^{noisy} and the corresponding ideal energies E^{ideal} .

We show the ideal energies and measured noisy energies in Fig. 21 along the optimisation iterations for H₂ (a), LiH (b) and F₂ (c) at all the bond distances. The measured noisy energies represent the measurement energies only with Readout Error Mitigation (REM). We observe that the ideal energies and measured energies have a well-linear dependence. The slope of the fitting curves gives us the depolarising fidelity p , which decreases with a deeper circuit.

To further our understanding of noise with an increasing circuit size, we compare the circuit fidelity estimated using different methods. As a reference, we calculate the circuit fidelity by multiplying the fidelity of each individual gate, which is obtained by individual XEB. Specifically, we first calculate the fidelity of each layer using the Pauli fidelity, and calculate the whole circuit fidelity using the depolarising fidelity of different layers. Since dynamical decoupling is used in our experiment to avoid dephasing during the idle time, we also take account of the idle time decay. The idle time fidelity is calculated by the fidelity of a single-qubit gate with an equal time length.

Fig. 21d shows the comparison of the estimation using individual XEB results with (red) and without idle time decay (blue), and the fitted depolarising fidelity by fitting the ideal energies and measured energies (orange). Remarkably, we can find that the actual circuit error rate is much lower than the error estimated with individual XEB results when the system size increases. This result implies the potential for the simulation of larger molecules. A detailed investigation will be an interesting future work.

E. Challenges

As we have discussed here and in the main text, there are many challenges in VQE experiments. Compared to dynamics simulation or random circuit sampling, VQE experiments are more challenging. The former examples only require running one instance on a quantum processor. In contrast, in the VQE experiment, the final results are highly related to the results that are obtained in the prior incidents. In spite of these challenges, our experiments for the first time achieved chemical accuracy for the six-qubit VQE simulation of molecular systems. Good control of hardware and efficient quantum algorithms enable such high-precision simulation.

For future large-scale quantum computational chemistry experiments, it is crucial to suppress gates and measurement readout errors in order to achieve chimerical accuracy with quantum hardware. We point out these challenges as follows.

Stability during experiments. For large-scale problems, VQE experiments could take several hours or days to obtain the ground state. Therefore, the performance of VQE highly depends on the stability of the experimental system. In our experiment, the readout error mitigation and Clifford fitting schemes are applied. These techniques require maintaining the system feature during the REM matrix extraction experiment, Clifford fitting experiment and VQE experiment. Only when the system float is suppressed can we make the error mitigation schemes work. The fluctuation mainly comes from the following:

1. **Electronic outcome fluctuation.** The electronic outcome determines the system conditions and manipulation accuracy, such as the qubit frequencies, coupler flux bias and the control pulse amplitude. The fluctuation of electronics directly affects gate fidelities as well as the results of the quantum circuit. The outcome accuracy of the electronic itself could be suppressed by increasing the samples, but the average outcome amplitude is greatly influenced by ambient temperature.

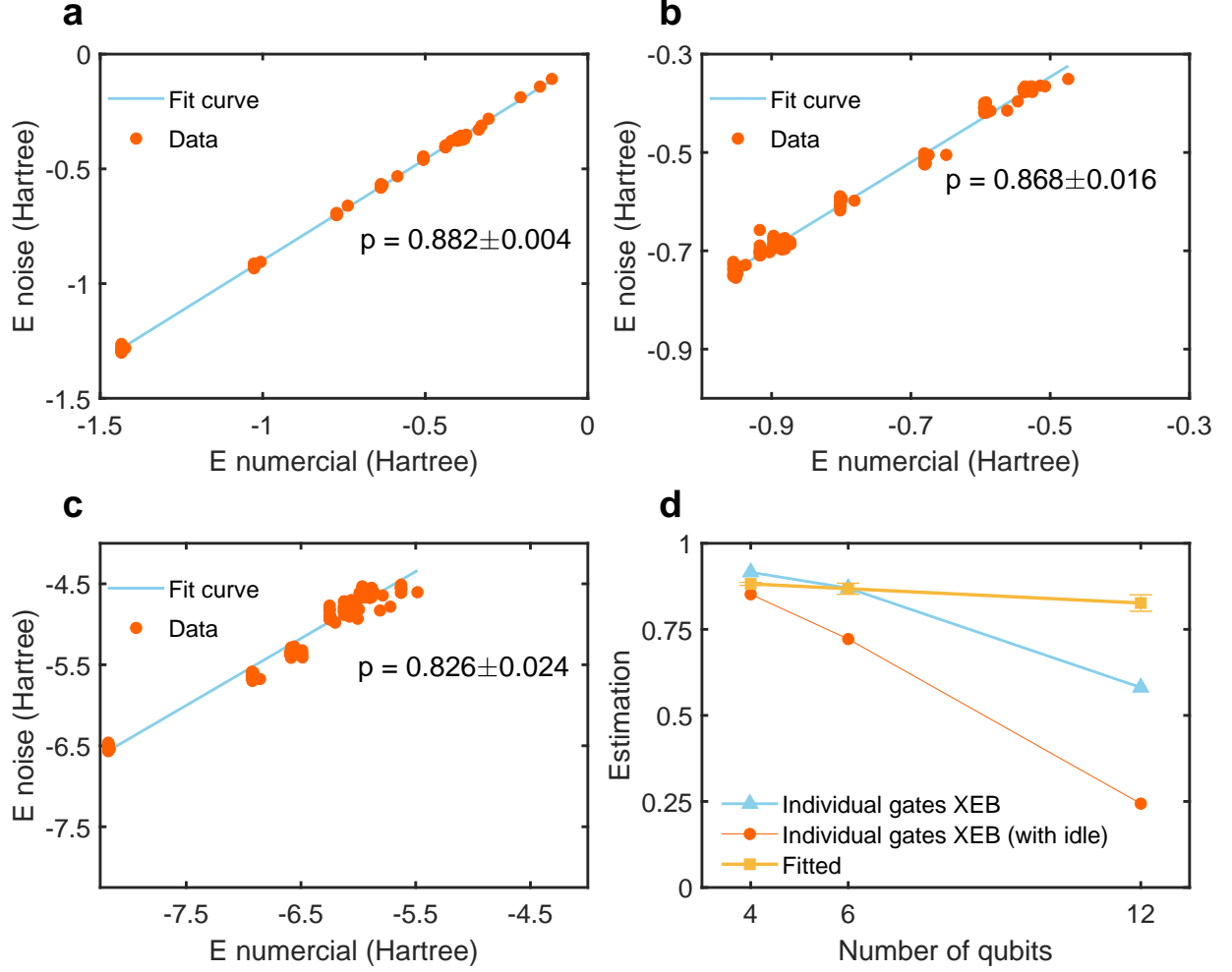


FIG. 21. **Fitted results using a depolarising noise model.** The figures show the ideal energies and measured energies along the optimisation iterations for H₂ (a), LiH (b) and F₂ (c) at all the bond distances. The noisy energies represent the measurement energies only with Readout Error Mitigation (REM). The ideal energies and measured energies have a linear dependence. The slope of the fitting curves characterises the depolarising fidelity p . (d) The circuit fidelity estimation by individual XEB results with and without idle time decay, and the fitted depolarising fidelity obtained by fitting the data points in (a)(b)(c).

2. Unstable Two Level System (TLSs). When the unstable TLSs near close to qubit operating frequency, the coherence of qubits would decrease abruptly. The noisy model changed which make the Clifford fitting fail.

Errors and samples. In our experiment, as we pointed out, we require the expectation values of observables for the optimisation and energy evaluation, instead of single-shot measurements. To suppress the statistical errors less than ϵ , the number of samples scales as $1/\epsilon^2$. With the increase of qubit number, coherent errors become a main error source, which leads to a large slope for the Clifford fitting function f^{CF} , as shown in Fig. 15, and hence a large variance. As a result of fitting, more samples are required for a larger system to suppress the fluctuation. Nevertheless, this can be overcome by further improving hardware performance. This is because a smaller error rate will lower the inherent expectation value variance, and hence fewer samples are required. In addition, the number of observable increases with the system size, and thus more samples are needed in a larger VQE experiment. This requires a long time to run experiments, and it could be hard to stabilise the system for a long time.